# PHOTOCATALYTIC DEGRADATION OF TETRACYCLINE WITH FeO$_x$/Fe- Bi$_2$O$_2$CO$_3$ SYNTHESIZED BY ONE-STEP HYDROTHERMAL METHOD

CHANIPHON   SUNKHUNTHOD

A Thesis Submitted in partial Fulfillment of the Requirements for the

Degree of Master of Science in Chemistry

Suranaree University of Technology

Academic Year 2023

# การสลายตัวด้วยการเร่งปฏิกิริยาเชิงแสงของเตตระไซคลีนด้วย FeO$_x$/Fe-Bi$_2$O$_2$CO$_3$ ที่สังเคราะห์โดยวิธีไฮโดรเทอร์มัลขั้นตอนเดียว
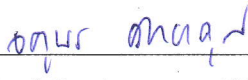
นางสาวชนิภรณ์  สูนขุนทด

# PHOTOCATALYTIC DEGRADATION OF TETRACYCLINE WITH

# FeO$_x$/Fe- Bi$_2$O$_2$CO$_3$ SYNTHESIZED BY ONE-STEP HYDROTHERMAL METHOD

Suranaree University of Technology has approved this thesis submitted in partial fulfillment of the requirements for a Master's Degree.
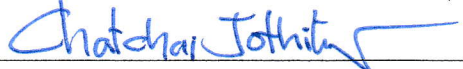
Thesis Examining Committee

_____

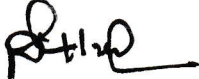(Prof. Dr. Jatuporn  Wittayakun)

Chairperson

_____

(Assoc. Prof. Dr. Theeranun  Siritanon)

Member (Thesis Advisor)

_____

(Assoc. Prof. Dr. Sanchai  Prayoonpokarach)

Member

_____

(Assoc. Prof. Dr. Rapee  Utke)

Member

_____  
(Assoc. Prof. Dr. Chatchai  Jothityangkoon)  
Vice Rector for Academic Affairs  
and Quality Assurance

_____  
(Prof. Dr. Santi  Maensiri)  
Dean of Institute of Science

ชนิภรณ์ สูนขุนทด : การสลายตัวด้วยการเร่งปฏิกิริยาเชิงแสงของเตตระไซคลีนด้วย $FeO_x$/Fe-$Bi_2O_2CO_3$ ที่สังเคราะห์โดยวิธีไฮโดรเทอร์มัลขั้นตอนเดียว (PHOTOCATALYTIC DEGRADATION OF TETRACYCLINE WITH $FeO_x$/Fe- $Bi_2O_2CO_3$ SYNTHESIZED BY ONE-STEP HYDROTHERMAL METHOD อาจารย์ที่ปรึกษา: รองศาสตราจารย์ ดร.ธีรนันท์ ศิริตานนท์, 55 หน้า.

คำสำคัญ: $Bi_2O_2CO_3$; การเจือ Fe; ตัวเร่งปฏิกิริยาเชิงแสง; เตตระไซคลีน; $FeO_x$

    ปฏิกิริยาตัวเร่งปฏิกิริยาเชิงแสง เป็นวิธีหนึ่งที่มีประสิทธิภาพในการลดการปนเปื้อนของยาปฏิชีวนะในน้ำ ซึ่งงานวิจัยนี้นำเสนอเกี่ยวกับวิธีการเตรียมและผลการย่อยสลายสารเตตระไซคลีนด้วยแสงของ $FeO_x$/Fe-$Bi_2O_2CO_3$ ด้วยวิธีไฮโดรเทอร์มัลขั้นตอนเดียว จากการทดลองพบว่า การเพิ่ม Fe ในโครงสร้างของ $Bi_2O_2CO_3$ ส่งผลให้เกิดการเติบโตของระนาบ {001} ซึ่งเป็นระนาบที่เหมาะสำหรับการเร่งปฏิกิริยาเชิงแสง และยังพบว่า ช่วงการดูดกลืนแสงเพิ่มขึ้นในช่วงแสงที่ตามองเห็น นอกจากนี้ $FeO_x$ ที่มีอนุภาคขนาดนาโนยังช่วยเพิ่มการดูดกลืนแสงและการถ่ายโอนประจุระหว่างผิวหน้าของตัวเร่งปฏิกิริยา และยิ่งไปกว่านั้น $FeO_x$ ยังทำหน้าที่เป็นตัวเร่งปฏิกิริยาในการดักจับอิเล็กตรอนและโฮลที่เกิดขึ้น ซึ่งช่วยลดการรวมตัวของพาหะ ดังนั้นผลจากการเจือ Fe และการเติม $FeO_x$ จึงสามารถเพิ่มประสิทธิภาพการย่อยสลายด้วยแสงของเตตระไซคลีนได้ถึง 2-3 เท่า เมื่อเทียบกับ $Bi_2O_2CO_3$ ที่ยังไม่มีการเจือ ดังนั้นงานวิจัยนี้นำเสนอตัวเร่งปฏิกิริยาเชิงแสงในระบบ $Bi_2O_2CO_3$ ที่เตรียมได้ง่ายและมีประสิทธิภาพสูงซึ่งจะเป็นประโยชน์ต่อการพัฒนาวัสดุอื่น ๆ ต่อไปในอนาคต

สาขาวิชาเคมี

ปีการศึกษา 2566

ลายมือชื่อนักศึกษา _____

ลายมือชื่ออาจารย์ที่ปรึกษา _____

CHANIPHON SUNKHUNTHOD : PHOTOCATALYTIC DEGRADATION OF TETRACYCLINE WITH FeO$_x$/Fe- Bi$_2$O$_2$CO$_3$ SYNTHESIZED BY ONE-STEP HYDROTHERMAL METHOD. THESIS ADVISOR : ASSOC. PROF. THEERANUN SIRITANON, Ph.D. 55 PP.

Keyword: Bi$_2$O$_2$CO$_3$; Fe-doped; Photocatalyst; Tetracycline; FeO$_x$

As an effective method to reduce the antibiotic contamination in water, photocatalysis has been widely investigated. Here, we report a preparation and tetracycline photodegradation of FeO$_x$/Fe-Bi$_2$O$_2$CO$_3$ system prepared from a one-step hydrothermal technique. Based on experiments and calculations, it is found that incorporation of Fe in Bi$_2$O$_2$CO$_3$ lattice results in a preferential growth of {001} facets, the active facets for photocatalytic reactions, and an increased light absorption in visible region. Additionally, FeO$_x$ nanoparticles increase light absorption and carriers' generation *via* an interfacial charge transfer. Moreover, FeO$_x$ act as cocatalysts to trap photogenerated electrons and holes, reducing the carriers' recombination. A combination of positive effects from both Fe doping and FeO$_x$ deposition could increase tetracycline photodegradation performance by two to three times comparing to the pristine Bi$_2$O$_2$CO$_3$. Thus, this work provides an easy to prepare and enhanced Bi$_2$O$_2$CO$_3$ – based photocatalysts, which could benefit the future development of other materials in the field.

School of Chemistry

Academic Year 2023

Student's Signature _Chaniphon Sunkhunthod._

Advisor's Signature _Theeranun Siritanon_

# ACKNOWLEDGMENTS

Chaniphon Sunkhunthod

# CONTENTS

# CONTENTS (Continued)

# LIST OF TABLES

# LIST OF FIGURES

# LIST OF FIGURES (Continued)

# LIST OF FIGURES (Continued)

# LIST OF ABBREVIATIONS AND SYMBOLS

| | |
|---|---|
| Rh B | Rhodamine B |
| TC | Tetracyclines |
| CTC | Chlortetracycline |
| OTC | Oxytetracycline |
| DC | Doxycycline |
| eV | electron volts |
| TOC | Total organic carbon |
| XRD | X-ray diffraction |
| XPS | X-ray photoelectron spectroscopy |
| TEM | Transmission Electron Microscope |
| SEM/EDS | Scanning Electron Microscope/ Energy Dispersive X-ray Spectroscopy |
| DRS | Diffused reflectance spectroscopy |
| PL | Photoluminescence Spectrometer |
| TGA | Thermogravimetric analysis |
| SAA | Surface Area Analyzer |
| HAADF | High-angle annular dark-field |
| BOC | $Bi_2O_2CO_3$ |
| HRTEM | High-resolution Transmission Electron Microscope |
| SAED | Selected-area electron diffraction |
| $\sigma$ | Surface energy |
| $E_{slab}$ | the total energy of the slab model |
| n | unit cell of bulk |
| $E_{bulk}$ | the total energy of the bulk unit cell |

# LIST OF ABBREVIATIONS AND SYMBOLS (Continued)

A             The surface area of the slab model

$C_0$         initial tetracycline concentration (mg/L)

$C_t$         tetracycline concentration at time

$k_{app}$     the rate constant of apparent pseudo first order

reaction ($min^{-1}$)

# CHAPTER I

# INTRODUCTION

## 1.1    Introduction

Organic pollutants are one of the main problems which are dangerous to human health. Tetracycline is the class of organic water pollutants, which are halogenated aliphatic and aromatic hydrocarbons. It is commonly used in the antibiotic industry and effective against infections caused by both Gram-positive and Gram-negative microorganisms. Tetracycline is a drug substance that is widely used in medicine because the price is low, and its high antibiotic activity. The structure of tetracycline is shown in Figure 1.1. The most common tetracyclines are tetracycline (TC), chlortetracycline (CTC), oxytetracycline (OTC) and doxycycline (DC) (Jeong et al., 2010).

| Compound | $R_1$ | $R_2$ | $R_3$ |
|---|---|---|---|
| Tetracycline (TC) | H | OH | H |
| Chlortetracycline (CTC) | Cl | OH | H |
| Oxytetracycline (OTC) | H | OH | OH |
| Doxycycline (DC) | H | H | OH |

**Figure 1.1** Structure of tetracyclines (Jeong et al., 2010).

Although the problems of tetracycline residues in environment are increasing, the general wastewater treatment is not designed to dispose of tetracycline antibiotics. Thus, there are many researches trying to develop effective methods. One of the popular methods for removing pollutants is heterogeneous photocatalysis. The photocatalytic degradation can completely oxidize the organic compounds to small molecules including $CO_2$ and $H_2O$ (Saadati, Keramati et al., 2016). Therefore, the photocatalytic degradation is interesting alternative to remove tetracyclines.

Semiconductor-based photocatalysts are considered as promising materials for degradation of organic pollutants, which are crucial for sustainable development considering environmental issues (Sheng-Peng Hu, 2014). One of the most interesting semiconductors is bismuth oxycarbonate ($Bi_2O_2CO_3$). It is a member of the bismuth oxide family based on the *Aurivillius* structure, consisting of $Bi_2O_2^{2+}$ layers alternated with $CO_3^{2-}$ layers (Álvarez et al., 2019; Dutta et al., 2020; Ka et al., 2017). Studying a comparison of $Bi_2O_2CO_3$ synthesis by the hydrothermal methods and solvothermal methods, Liu et al. found that both methods exhibited different morphologies. The $Bi_2O_2CO_3$ synthesized by solvothermal method has smaller particle than $Bi_2O_2CO_3$ synthesized by hydrothermal method. $Bi_2O_2CO_3$ synthesized by solvothermal method has higher photocatalytic performance for Rh B degradation than $Bi_2O_2CO_3$ synthesized by hydrothermal method because the band gab energy has narrowed (Liu et al., 2010). However, the hydrothermal method is more environmentally friendly than the solvothermal method. $Bi_2O_2CO_3$ exhibits good photocatalytic degradation performance under UV light irradiation. However, it can only be excited by UV light because it is a wide-band-gap semiconductor. One method to enhance the absorption in visible light region is doping. The cationic doping such as Zn increases the specific surface area and decreases the band gap energy of $Bi_2O_2CO_3$. Therefore, it enhances photodegradation efficiency of methylene blue (Yaqoob et al., 2020).  The anionic doping such as Cl (Connell, Wu et al., 2006; Li, Ren et al., 2020), Br (Zhang et al., 2018), and I (Jiantao Zai, 2016) also decreases the width of the energy band gap, thereby increasing the efficiency of photocatalytic activity under visible light.

Fe doping into bismuth oxycarbonate was prepared with the solvothermal method. Fe was doped in $Bi_2O_2CO_3$ at v (W.Connell et al., 2006) various Fe amounts of 0, 0.02, 0.05, 0.10 and 0.15 g that can be calculated to 3,8,16.7 and 25 mol%, respectively. It was found that 16.7 mol% Fe in $Bi_2O_2CO_3$ showed the best performance for Rh B photodegradation. The improvement was a result of reduced band gap energy of $Bi_2O_2CO_3$ after Fe doping, which improves light absorption in the visible region and therefore enhances the photocatalytic activity (Li et al., 2018). On the other hand, higher Fe content slightly lower the efficiency as Fe can act as the recombination center.

While it was shown that Fe doping significantly reduce the band gap energy of $Bi_2O_2CO_3$, the effects of higher Fe content on the activity is unclear. Moreover, the previous work only tests the catalysts for Rh B degradation. Thus, this research aims to explore the system of Fe- $Bi_2O_2CO_3$ prepared by a hydrothermal method in a more systematic and detail investigation. Solubility of Fe in $Bi_2O_2CO_3$ structure was studied. Crystal structure of the samples was analyzed and the prepared catalysts was tested for tetracycline degradation.

## 1.2   References

Álvarez, L., Gascue, B. R. d., Tremont, R. J., Márquez, E., and Velazco, E. J. (2019). Synthesis and Characterization of a New Aluminum-Doped Bismuth Subcarbonate. *Crystals, 9*(466), 1-10.

Dutta, V., Sharma, S., Raizada, P., Kumar, R., Thakur, V. K., Nguyen, V.-H., Abdullah M. Asiri, Khan, A. A. P., and Singh, P. (2020). Recent progress on bismuth-based Z-scheme semiconductor photocatalysts for energy and environmental applications. *Journal of Environmental Chemical Engineering, 8*, 104505.

Jeong, J., Song, W., Cooper, W. J., Jung, J., and Greaves, J. (2010). Degradation of tetracycline antibiotics: Mechanisms and kinetic studies for advanced oxidation/reduction processes. *Chemosphere, 78*, 533–540.

Jiantao Zai, F. C., Na Liang, Ke Yu, Yuan Tian, Huai Sun, Xuefeng Qian. (2016). Rose-like I-doped Bi2O2CO3 microspheres with enhanced visible light response: DFT

calculation, synthesis and photocatalytic performance. *Journal ofHazardous Materials*.

Ka, P., Maji, T. K., Nandi, R., Lemmens, P., and Pal, S. K. (2017). In-Situ Hydrothermal Synthesis of Bi–Bi$_2$O$_2$CO$_3$ Heterojunction Photocatalyst with Enhanced Visible Light Photocatalytic Activity. *Nano-Micro Letters, 9*.

Li, J., Liu, Y., Zhou, Y., Liu, S., Liang, Y., Luo, T., and Dai, G. (2018). Enhanced visible-light photocatalytic activity of Bi$_2$O$_2$CO$_3$ nanoplates by Fe-doping in the degradation of rhodamine B. *Materials Research Bulletin, 107*, 438-445.

Liu, Y., Wang, Z., Huang, B., Yang, K., Zhang, X., Qin, X., and Dai, Y. (2010). Preparation, electronic structure, and photocatalytic properties of Bi$_2$O$_2$CO$_3$ nanosheet. *Applied Surface Science, 257*, 172–175.

Sheng-Peng Hu, C.-Y. X., Bao-You Zhang, Yi Pei, and Liang Zhen. (2014). Solvothermal Synthesis of Bi2O2CO3 Nanoplates for Efficient Photodegradation of RhB and Phenol under Simulated Solar Light Irradiation. *Bull. Korean Chem. Soc., 35*(10), 2935-2940.

Yaqoob, A. A., Parveen, T., Umar, K., and Ibrahim, M. N. M. (2020). Role of Nanomaterials in the Treatment of Wastewater: A Review. *Water, 12*.

Zhang, G.-Y., Wang, J.-J., Shen, X.-Q., Wang, J.-J., Wang, B.-Y., and Gao, D.-Z. (2018). Br-doped Bi$_2$O$_2$CO$_3$ nanosheets with improved electronic structure and accelerated charge migration for outstanding photocatalytic behavior. *Applied Surface Science, 470*, 63-73.

# CHAPTER II

# LITERATURE REVIEW

## 2.1 Organic pollutants

Organic pollutants are known to be natural toxins, which are often found in water. Examples of organic water pollutants include volatile organic compounds and polynuclear aromatic hydrocarbons. Various classes of organic water pollutants and their sources are summarized in Table 2.1.

**Table 2.1** Major sources of organic pollutants in water (Beniah et al., 2019).

| Chemical class | Sources |
|---|---|
| Aliphatic and aromatic hydrocarbons (including benzenes, phenols and petroleum hydrocarbons) | Petrochemical industry wastes, Heavy/fine chemical industry wastes, Industrial solvent wastes, resins, synthetic fibers, rubbers and paints production, Coke oven and coal gasification plant effluents, Urban run-off, |
| Polynuclear aromatic hydrocarbons (PAHs) | Urban run-off, Petrochemical industry wastes, Various high temperature pyrolytic processes, Bitumen production, Electrolytic aluminum smelting, Coal-tar coated distribution pipes |
| Halogenated aliphatic and aromatic hydrocarbons | Disinfection of water and water, Heavy/fine chemicals industry wastes, Industrial solvent wastes and dry-cleaning wastes, Plastics, resins, synthetic fibers, rubbers and paints production, Heat-transfer, Aerosol propellants, Fumigants |

**Table 2.1** Major sources of organic pollutants in water (Beniah et al., 2019).

| Chemical class | Sources |
| --- | --- |
| Organochlorinated biphenyls | Agricultural run-off, Domestic usage, Pesticide production, Carpet mothproofing, Timber treatment |
| Polychlorinated biphenyls | Capacitor and transformer manufacture, Disposal of hydraulic fluids and lubricants, Waste carbonless copy paper recycling, Heat transfer fluids, Investment casting industries PCB production |
| Phthalate esters | Plastics, resins, synthetic fibers, rubbers and paints production, Heavy/fine chemicals industry wastes, Synthetic polymer distribution pipes |

Due to its widespread use, tetracycline can become an environmental contaminant. Many antibiotics are excreted in the urine and feces from humans and animals that used the antibiotic drugs. When it is released, it will contaminate the soil and water and cause potential risks to environment and human health (Banik and Hossain, 2006). Residues from tetracycline antibiotics are not good for the ecosystem and are toxic to human health when they are in drinking water or used water to wash fruits and vegetables. These antibiotics agents interfere with the intestinal microflora of humans and animals, making it more prone to other infections. In fact, it has been reported that even the residual antibiotics can cause genetic variant that results in the antibiotic resistant pathogen (Chee-Sanford et al., 2001).

Although the problems of tetracycline residues in environment are increasing, the general wastewater treatment is not designed to dispose of tetracycline antibiotics. Thus, there are many researches trying to develop effective methods. One of the popular methods for removing pollutants is heterogeneous photocatalysis. The photocatalytic degradation can completely oxidized the organic compounds to small

molecules including $CO_2$ and $H_2O$ (Saadati et al., 2016). Therefore, the photocatalytic degradation is interesting alternative to remove tetracyclines.

## 2.2 Photocatalytic property

Photo means light and a catalyst are a substance that increases the reaction rate without affecting itself. Therefore, a photocatalyst is a catalyst that enhances the reaction by absorbing energy from light. Photocatalysts are often applied in water splitting and organic degradation.

### 2.2.1 Photocatalytic reaction

Most photocatalysts are semiconductors. A semiconductor consists of conduction band and valence band that are separated by a gap between them. This gap is called the band gap. When photocatalysts absorb the light energy greater than the band gap energy, electrons and holes are created in the conduction band and the valence band, respectively. The main factor influencing the absorbance in semiconductor photocatalysts is the band gap energy. The photocatalytic processes are effective to use solar energy to drive chemical reactions, but most semiconductor photocatalysts can be activated only by UV light. However, the solar light or solar spectrums has only 5% UV light but as high as 50% visible light. Therefore, extending the absorption region from UV light region to visible light region would significantly increase the catalysts' efficiency (Molinari et al., 2020).
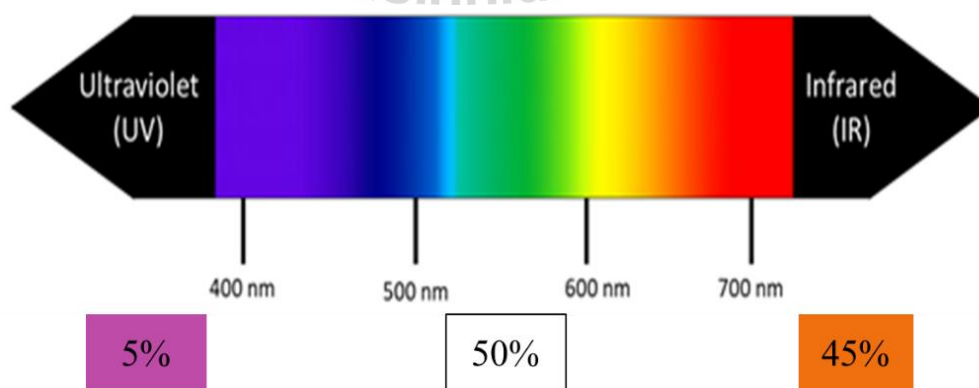


**Figure 2.1** Electromagnetic spectrum of sunlight (Lee).

Once the electrons and holes are created, two competitive events can occur. The electrons and holes either recombine or migrate to react at the surface. Recombination of charge carriers would decrease the active species and consequently decrease photocatalytic activity. Thus, charge separation and transport are very important in photocatalysis. Carrier transport depends on the crystallinity and particle size. Since defects could act as recombination centers, catalysts with high crystallinity and lower defects are preferred. On the other hand, if the particle size is small, the distance that electrons and holes must travel to the surface for the reaction is shortens, which reduce the recombination rate. The electrons and holes produced by light react in redox reactions at the surface of the catalysts as shown in Figure 2.3. These carriers must also have appropriate potential for the reactions. For example, the potential at the conduction band minimum must be more negative than the redox potential of $H^+/H_2$ while the maximum of the valence band must be more positive than the redox potential of $O_2/H_2O$ so that electrons and holes can split the water molecules to $H_2$ and $O_2$. Figure 2.4 show the relative potentials of conduction bands and valence bands of various known photocatalysts for water splitting (Kudo and Miseki, 2009).
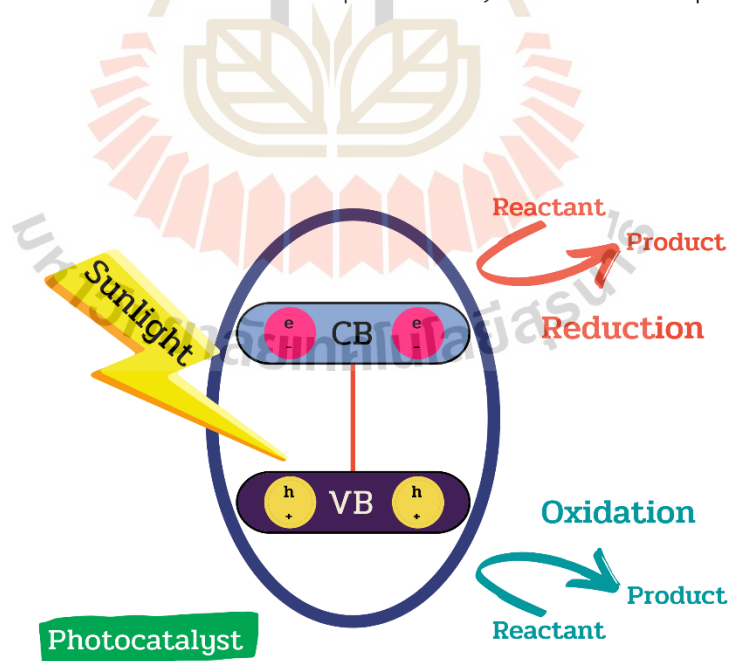


**Figure 2.2** The scheme of photocatalytic process of semiconductor.
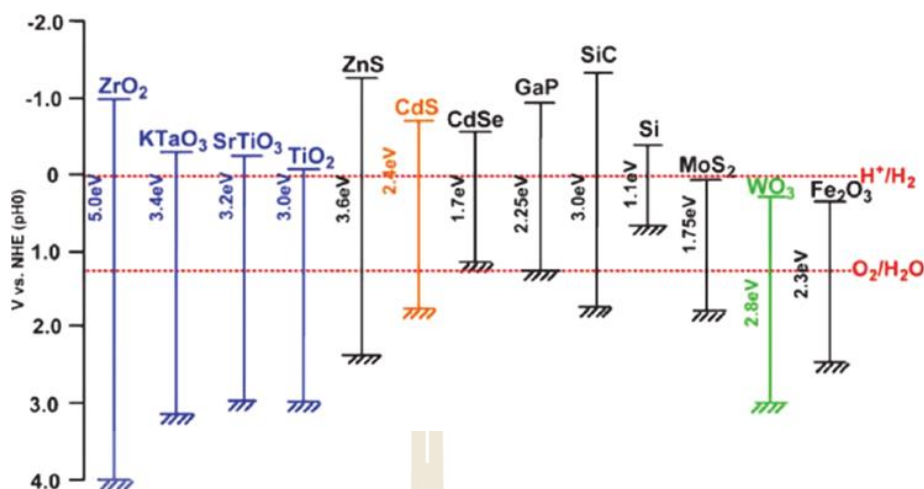
**Figure 2.3** Redox potential of water splitting.

Photocatalytic reactions of organic pollutants degradation occur in a similar way to the process of water splitting. The photocatalysts will absorb the light to create electrons and holes. The electrons and holes in the conduction band and valance band will then react on the surface of the sample. In most cases, the electrons react with water to form a hydroxyl radical, and holes react with $O_2$ to form a superoxide radical. The hydroxyl radical and the superoxide radical will react with the organic pollutant causing degradation and mineralization as shown in Figure 2.5m (Yaqoob et al., 2020).
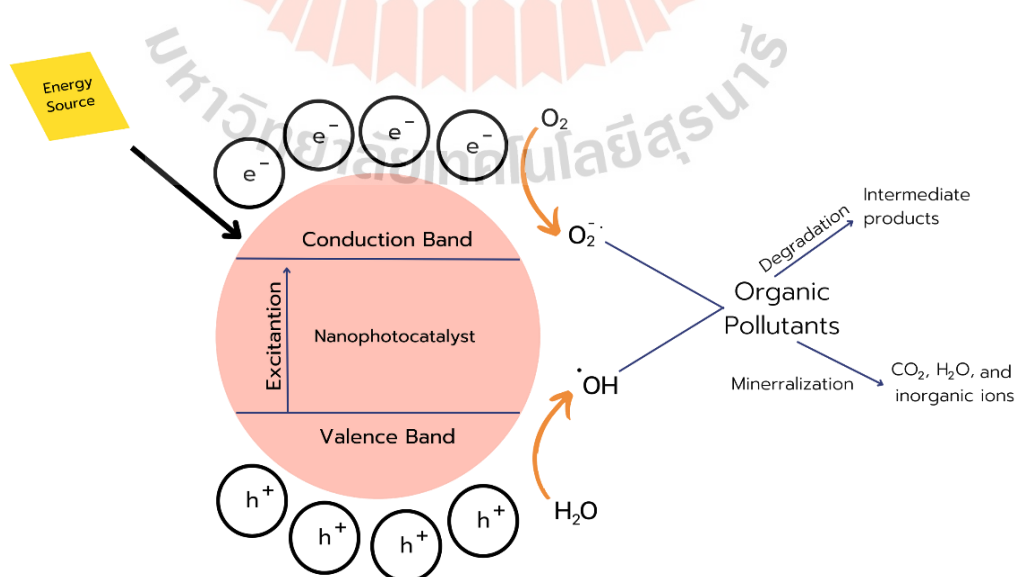


**Figure 2.4** The scheme of organic pollutant compound degradation.

### 2.2.2 Strategies to improve photocatalytic activity

Photocatalysis is an efficient process for removing organic contaminants, it is one of the most used alternatives to degrade environmental contamination. However, the photocatalyst materials have some limitations for photocatalytic activity such as: width of band gab energy and electron-hole pair recombination rate. (Ansari et al., 2019; Molinari et al., 2020) Thus, the researchers are trying to develop materials and improve photocatalytic activity. Here, two examples of the most used strategies are discussed: doping and making composites.

#### 2.2.2.1 Doping

Doping is a modification of photocatalysts. It could reduce the gap between the conduction band and the valence band by adding impurities like metals and non-metals. The specific effects on various semiconductors differ. In many cases, addition of metals and non-metals enhance the photocatalyst by lowering the band gap energy and increasing visible light absorption as new energy bands are created. For example, doping Ag, Ni, Co, Au, Cu, V, Ru, Fe, La, Pt, Cr, and Ce in titanium dioxide increase the catalysts' performances under visible light due to the extended light absorption from UV region to visible light region (Mogal et al., 2013).

In addition, the addition of contaminants in photocatalysts can improve efficiency by: (Ameta et al., 2018)

➢ Lowering hole-electron aggregation.
➢ Increasing surface area.
➢ Increasing the pore size.
➢ Increasing the crystallinity.

#### 2.2.2.2 Coupled semiconductors or Composites

The composites are the coupling of semiconductors. It is another efficient method for semiconductors to increase light absorption in the visible region. The composites can consist of a large band gap semiconductor and a small band gap

semiconductor. The electrons from a conduction band transfer from a semiconductor with small band gap to the one with larger band gap. For the example, $FeTiO_3/TiO_2$, $Ag_3PO_4/TiO_2$, $W_{18}O_{49}/TiO_2$, $CdS/TiO_2$, $CdSe/TiO_2$, $NiTiO_3/TiO_2$, $CoTiO_3/TiO_2$, $Fe_2O_3/TiO_2$ (Banik and Hossain, 2006; W.Connell et al., 2006), $ZnO/CdS$, $TiO_2/SnO_2$ (Yaqoob et al., 2020), $ZnO/TiO_2$ and $ZnO/Ag_2S$ (Chee-Sanford et al.) are reported for effective photocatalysts. In these cases, recombination of the electron-hole pairs are also reduced, which help enhancing the photocatalytic performance. (Ameta et al., 2018)

## 2.3    Bismuth oxycarbonate ($Bi_2O_2CO_3$)

This section focuses on the bismuth oxycarbonate ($Bi_2O_2CO_3$) and doping in bismuth oxycarbonate ($Bi_2O_2CO_3$).

Bismuth oxycarbonate ($Bi_2O_2CO_3$) consists of an alternating $Bi_2O_2^{2+}$ layer and a $CO_3^{2-}$ layer. Bismuth oxycarbonate can adopt either a tetragonal or orthorhombic structure with a body-centered atomic arrangement. The crystal structures of $Bi_2O_2CO_3$ are depicted in Figure 2.5 (Zheng et al., 2010).  In detail, the structure is built up of a highly distorted Bi-O units, where   $Bi^{3+}$ atom is coordinated by 8 oxygens, resulting in stereo dynamic lone-pair character in the local structure of the compound. Such behavior benefits for photocatalytic properties because this kind of structure contains many oxygen defects and promote the rapid formation of electron pairs. Therefore, $Bi_2O_2CO_3$ was reported with an excellent photocatalytic activity in many works (Cheng et al., 2010; Zhao et al., 2011). However, its relatively large band gap of 3.0-3.6 eV causes poor light absorption properties, especially in the visible light (Zheng et al., 2010).
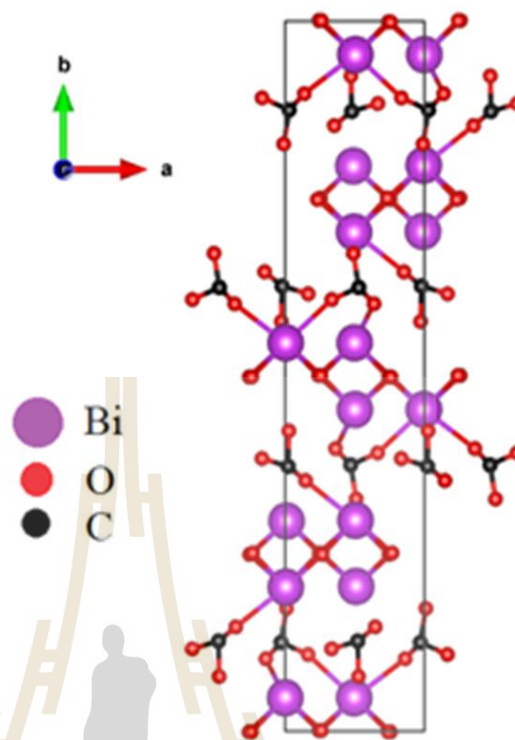
**Figure 2.5** The crystal structure of the $Bi_2O_2CO_3$ in orthorhombic phase.

Bismuth oxycarbonate can have different morphologies, which gives different properties. For example, Huang et al. (2014), compared the activity of $Bi_2O_2CO_3$ microspheres and $Bi_2O_2CO_3$ nanoplates. The degradation efficiency of rhodamine B (RhB) of $Bi_2O_2CO_3$ nanoplates are more than the $Bi_2O_2CO_3$ microsphere because the $Bi_2O_2CO_3$ nanoplates have good charge separation properties. (Huang et al., 2015)  In addition, Peng et al. compared salicylic acid (SA) degradation of $Bi_2O_2CO_3$ nanorods and $Bi_2O_2CO_3$ nanoplates. $Bi_2O_2CO_3$ nanorods had better total organic carbon (TOC) removal of SA than $Bi_2O_2CO_3$ nanoplates because their absorbance range was improved from UV light to visible light which enhanced photocatalytic performance (Peng et al., 2021). Examples of the various morphologies of $Bi_2O_2CO_3$ are microsphere, nanoplates (Huang et al., 2015) and nanorods (Peng et al., 2021).

## 2.4    Fabrication of $Bi_2O_2CO_3$

Bismuth oxycarbonate can be fabricated by various techniques such as wet-chemical method, template-free method, reflux method, ion-exchange method, solvothermal method and hydrothermal method. However, the most used methods are hydrothermal and solvothermal because they can be completed in a short time (Dutta et al., 2021).

Studying a comparison of $Bi_2O_2CO_3$ synthesis by the hydrothermal methods and solvothermal methods, Liu et al. found that both methods exhibited different morphologies. The $Bi_2O_2CO_3$ synthesized by solvothermal method has smaller particle than $Bi_2O_2CO_3$ synthesized by hydrothermal method. It was found that $Bi_2O_2CO_3$ synthesized by solvothermal method has higher photocatalytic performance for Rh B degradation because the band gab energy has narrowed (Liu et al., 2010). However, the hydrothermal method is more environmentally friendly than the solvothermal method.

## 2.5    Strategies to improve photocatalytic activities of $Bi_2O_2CO_3$

### 2.5.1 Heterojunction formation

Semiconductor heterojunctions are formed by two semiconductors. The two semiconductors mush have appropriated conduction band and valence band positions and energy bandgap. Heterojunction formation enhances photocatalytic activity because it increases the separation of generated charges. Examples of heterojunctions consisting bismuth oxycarbonate are $BiVO_4/Bi_2O_2CO_3$ (Madhusudan et al., 2011), $Bi_2O_2CO_3/BiMoO_6$ (Zhang et al., 2019), $BiOCl/Bi_2O_2CO_3$ (Xie et al., 2019), $Bi_2O_2CO_3$/porous $g\text{-}C_3N_4$ (Duan et al., 2019). The heterojunctions can be classified as shown in Figure 2.6 (Li et al., 2021).
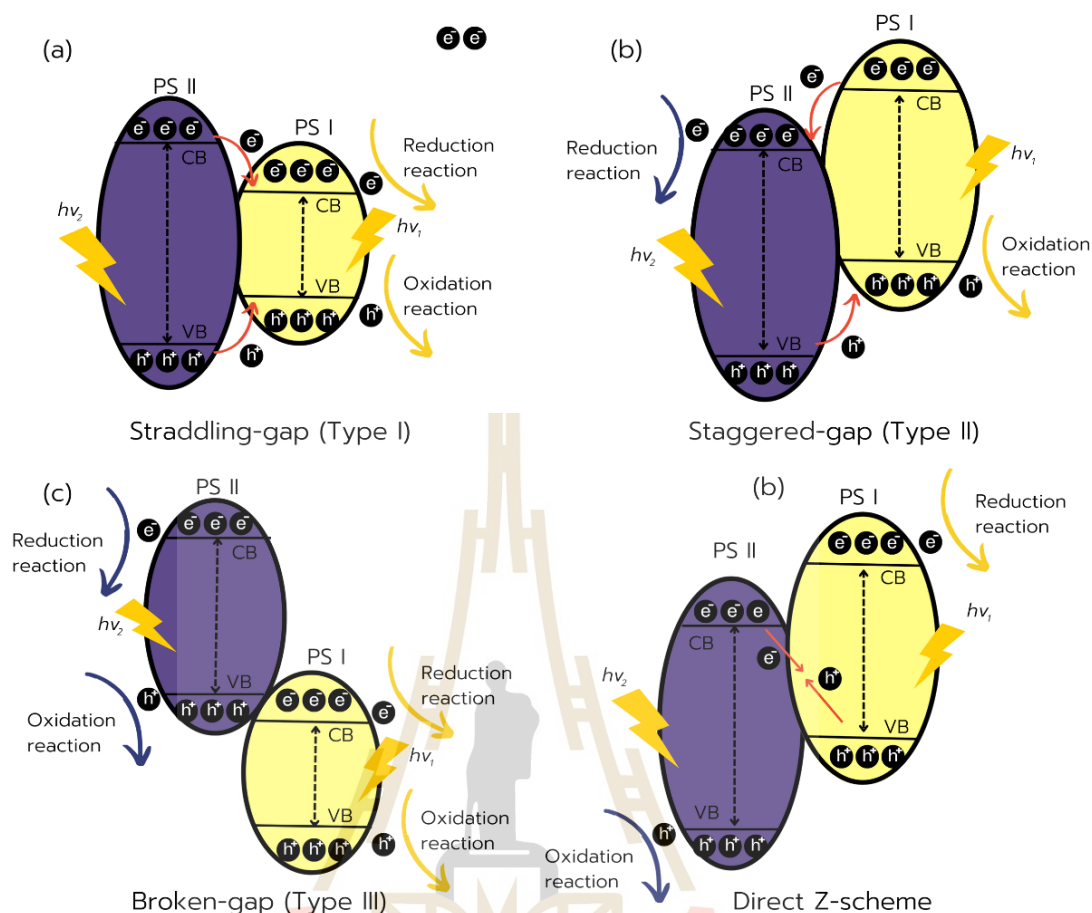
**Figure 2.6** The types of heterojunctions: (a) Type I, (b) Type II, (c) Type III and (d) direct Z-scheme heterojunction.

**Straddling-gap (Type I):** The electrons and hole are gathered in semiconductor with smaller bandgap, resulting in a fast recombination rate and a poor photocatalytic activity.

**Staggered-gap (Type II):** The electrons are gathered at conduction band of photosystem II (PS II) and the holes are gathered at valance band of photosystem I (PS I). Therefore, Type II heterojunction enhances the photocatalytic performance due to a high separation of charge carriers. For example, Qiu et al., prepared $Bi_2O_2CO_3$/BiOBr p-n heterojunction with improved Rh B photodegradation (Qiu et al., 2017). However, in type II heterojunction, the electrons and holes are gathered at bands with low energy potential which means that the redox capacities can be reduced.

**Broken-gap (Type III):** The electrons and holes are not transferred between the two semiconductors; they are gathered in the original photosystems. The two photosystems will work separately without any furtherance.

**Direct Z-scheme:** The band stagger of direct Z-scheme is similar to that of Type II heterojunctions but they have different charge transfer. The electrons move from photosystems I to photosystems II and holes move from photosystems II to photosystems I. The direct Z-scheme enhances redox capacities for the photocatalytic reaction. For example, Li et al. has proposed a z-scheme heterojunction of $WS_2/Bi_2O_2CO_3$. The heterojunction has higher degradation efficiency for LR5B and CIP compared to $WS_2$ and $Bi_2O_2CO_3$ (Li et al., 2019).

### 2.5.2 Doping

It is known that the photocatalytic activity of the semiconductor depends on the light absorption, oxidation power, and separation efficiency of photogenerated electron-hole pairs. It has been reported that doping is an effective strategy to improve these factors. The cationic doping such as B (Zhang et al., 2021), Al (Álvarez et al., 2019), Ni (Amadu et al., 2021) and Zn increases the specific surface area and decreases the band gap energy of $Bi_2O_2CO_3$. Therefore, it enhances photodegradation efficiency of methylene blue (Yaqoob et al., 2020). The anionic doping such as Cl (Li et al., 2020; W.Connell et al., 2006), Br (Zhang et al., 2018), F (Liu et al., 2020) and I (Jiantao Zai, 2016) also decrease the width of the energy band gap, thereby increasing the efficiency of photocatalytic activity under visible light.

Fe doping into bismuth oxycarbonate was prepared with the solvothermal method (Li et al., 2018) . Fe was doped in $Bi_2O_2CO_3$ at various Fe amounts of 0, 0.02, 0.05, 0.10 and 0.15 g that can be calculated to 3,8,16.7 and 25 mol%, respectively. It was found that 16.7 mol% Fe in $Bi_2O_2CO_3$ showed the best performance for Rh B photodegradation. The improvement was a result of reduced band gap energy of $Bi_2O_2CO_3$ after Fe doping, which improves light absorption in the visible region and therefore enhances the photocatalytic activity (Figure 2.13). On the other hand, higher Fe content slightly lower the efficiency as Fe can act as the recombination center.

## 2.6 References

Álvarez, L., Gascue, B. R. d., Tremont, R. J., Márquez, E., and Velazco, E. J. (2019). Synthesis and Characterization of a New Aluminum-Doped Bismuth Subcarbonate. *Crystals, 9*(466), 1-10.

Amadu, B. D., Xu, D., Zhang, Q., Zhang, Z., Wang, Q., Dong, Y., Zhang, G., Rena, Z., and Wang, P. (2021). Synthesis of ultrathin, porous and surface modified $Bi_2O_2CO_3$ nanosheets by Ni doping for photocatalytic organic pollutants degradation. *Journal of the Taiwan Institute of Chemical Engineers, 125*, 78-87.

Ameta, R., Solanki, M. S., Benjamin, S., and Amet, S. C. (2018). Advanced Oxidation Processes for Wastewater Treatment. *Emerging Green Chemical Technology*, 135-175.

Ansari, M. O., Kumar, R., Ansari, S. P., Hassan, M. S. A.-w., Alshahrie, A., and Barakat, M. A. E.-F. (2019). Nanocarbon aerogel composites. *Nanocarbon aerogel composites*, 1-26.

Banik, K. K., and Hossain, S. (2006). Pharmaceuticals in drinking water: a future water quality threat. *Indian Journal of Environmental Protection, 26*, 926–932.

Beniah, I., Obinnaa, and Ebere, E. C. (2019). A Review: Water pollution by heavy metal and organic pollutants: Brief review of sources, effects and progress on remediation with aquatic plants. *Analytical Methods in Environmental Chemistry, 2*(3), 5-38.

Chee-Sanford, J. C., Aminov, R. I., Krapac, I. J., Garrigues-Jeanjean, N., and Mackie, R. I. (2001). Occurrence and diversity of tetracycline resistance genes in lagoons and groundwater underlying two swine production facilities. *Applied and Environmental Microbiology, 67*, 1494–1502.

Cheng, H., Huang, B., Yang, K., Wang, Z., Qin, X., Zhang, X., and Dai, Y. (2010). Facile Template-Free Synthesis of $Bi_2O_2CO_3$ Hierarchical Microflowers and Their Associated Photocatalytic Activity. *ChemPhysChem, 11*, 2167– 2173.

Duan, Y., Li, J., Li, Y., Shang, X., Jia, D., and Li, C. (2019). Direct Z-scheme $Bi_2O_2CO_3$/porous g-$C_3N_4$ heterojunction for improved photocatalytic degradation performance. *Journal of the Taiwan Institute of Chemical Engineers*.

Dutta, V., Sharma, S., Raizada, P., Aslam, A., Khan, P., Asiri, A. M., Nadda, A., Singh, P., Le, Q. V., Huang, C.-W., Nguyen, D. L. T., Pansambal, S., and Nguyen, V.-H. (2021). Rescent advances and emerging trends in $(BiO)_2CO_3$ base photocatalysts for environmental remediation: A review. *Surfaces and Interfaces, 25*.

Huang, H., Wang, J., Dong, F., Guo, Y., Tian, N., Zhang, Y., and Zhang, T. (2015). Highly Efficient $Bi_2O_2CO_3$ Single-Crystal Lamellas with Dominantly Exposed {001} Facets. *Crystal Growth & Design, 15*, 534–537.

Jiantao Zai, F. C., Na Liang, Ke Yu, Yuan Tian, Huai Sun, and Xuefeng Qian. (2016). Rose-like I-doped Bi2O2CO3 microspheres with enhanced visible light response: DFT calculation, synthesis and photocatalytic performance. *Journal ofHazardous Materials*.

Kudo, A., and Miseki, Y. (2009, 8th October 2008). Heterogeneous photocatalyst materials for water splitting. *Chemical Society Reviews, 38*, 253–278.

Lee, A. *The EM Spectrum*. Retrieved 24/04/2022 from https://pressbooks.bccampus.ca/lightingforelectricians/chapter/the-em-spectrum/

Li, J.-h., Ren, J., Liu, Y., Mu, H.-y., Liu, R.-h., Zhao, J., Chen, L.-j., and Li, F.-t. (2020). In-situ synthesis of Cl-doped $Bi_2O_2CO_3$ and its enhancement of photocatalytic activity by inducing generation of oxygen vacancy. *INORGANIC CHEMISTRY FRONTIERS, 7*, 2969-2978.

Li, J., Liu, Y., Zhou, Y., Liu, S., Liang, Y., Luo, T., and Dai, G. (2018). Enhanced visible-light photocatalytic activity of $Bi_2O_2CO_3$ nanoplates by Fe-doping in the degradation of rhodamine B. *Materials Research Bulletin, 107*, 438-445.

Li, L., Cai, J., Yan, Y., Zhao, F., and Zhou, J. (2019). Flower-like direct Z-scheme $WS_2/Bi_2O_2CO_3$ photocatalyst with enhanced photocatalytic activity. *Journal of Alloys and Compounds, 810*(151872).

Li, X., Garlisi, C., Guan, Q., Anwer, S., Al-Ali, K., Palmisano, G., and Lianxi Zheng. (2021). A review of material aspects in developing direct Z-scheme photocatalysts. *Materials Today, 47*, 75-107.

Liu, Y., Wang, Z., Huang, B., Yang, K., Zhang, X., Qin, X., and Dai, Y. (**2010**). Preparation, electronic structure, and photocatalytic properties of $Bi_2O_2CO_3$ nanosheet. *Applied Surface Science, 257*, 172–175.

Liu, Z., Gu, W., Teng, F., Yang, X., and Jiang, W. (2020). Facile synthesis and greatly improved photocatalytic activity of $F-Bi_2O_2CO_3$ nanotubes with novel hierarchical wall. *Journal of Fluorine Chemistry, 236*(109557).

Madhusudan, P., Ran, J., Zhang, J., Yu, J., and Liub, G. (2011). Novel urea assisted hydrothermal synthesis of hierarchical $BiVO_4/Bi_2O_2CO_3$ nanocomposites with enhanced visible-light photocatalytic activity. *Applied Catalysis B: Environmental, 110*, 286-295.

Mogal, S. I., Mishra, M., Gandhi, V. G., and Tayade, R. J. (2013). Metal Doped Titanium Dioxide: Synthesis and Effect of Metal ions on Physico-chemical and Photocatalytic properties *Materials Science Forum, 734*, 364-378.

Molinari, R., Lavorato, C., and Argurio, P. (2020). Visible-Light Photocatalysts and Their Perspectives for Building Photocatalytic Membrane Reactors for Various Liquid Phase Chemical Conversions. *Catalysts, 10*(1334).

Peng, Y., Liu, M.-Q., Zhao, N.-N., and Kan, P.-F. (2021). Controlled synthesis of $Bi_2O_2CO_3$ nanorods with enhanced photocatalytic performance. *CrystEngComm*.

Qiu, F., Li, W., Wang, F., Li, H., Liu, X., and Ren, C. (2017). Preparation of novel p-n heterojunction $Bi_2O_2CO_3/BiOBr$ photocatalysts with enhanced visible light photocatalytic activity. *Colloids and Surfaces A: Physicochemical and Engineering Aspects, 517*, 25–32.

Saadati, F., Keramati, N., and Ghazi, M. M. (2016). Influence of parameters on the photocatalytic degradation of tetracycline in wastewater: A review. *CRITICAL REVIEWS IN ENVIRONMENTAL SCIENCE AND TECHNOLOGY, 0*, 1–26.

Xie, J., Guo, N., Liu, A., Cao, Y., Hu, J., and Jia, D. (2019). Simple solid-state synthesis of $BiOCl/Bi_2O_2CO_3$ heterojunction and its excellent photocatalytic degradation of RhB. *Journal of Alloys and Compounds, 784*, 377-385.

Yaqoob, A. A., Parveen, T., Umar, K., and Ibrahim, M. N. M. (2020). Role of Nanomaterials in the Treatment of Wastewater: A Review. *Water, 12*.

Zhang, G.-Y., Wang, J.-J., Shen, X.-Q., Wang, J.-J., Wang, B.-Y., and Gao, D.-Z. (2018). Br-doped $Bi_2O_2CO_3$ nanosheets with improved electronic structure and accelerated charge migration for outstanding photocatalytic behavior. *Applied Surface Science, 470*, 63-73.

Zhang, J., Cui, W., Chen, P., Li, K., Wua, H., and Dong, F. (2021). B doped $Bi_2O_2CO_3$ hierarchical microspheres: Enhanced photocatalytic performance and reaction mechanism for NO removal. *Catalysis Today, 380*, 230-236.

Zhang, J., Liu, Z., and Ma, Z. (2019). Facile Formation of $Bi_2O_2CO_3$/$Bi_2MoO_6$ Nanosheets for Visible LightDriven Photocatalysis. *ACS Omega, 4*, 3871–3880.

Zhao, T., Zai, J., Xu, M., Zou, Q., Su, Y., Wanga, K., and Qian, X. (2011). Hierarchical $Bi_2O_2CO_3$ microspheres with improved visible-light-driven photocatalytic activity. *CrystEngComm, 13*, 4010–4017.

Zheng, Y., Duan, F., Chen, M., and Xie, Y. (2010). Synthetic $Bi_2O_2CO_3$ nanostructures: Novel photocatalyst with controlled special surface exposed. *Journal of Molecular Catalysis A: Chemical, 317*, 34–40.

# CHAPTER III

# EXPERIMENTAL

## 3.1    Chemicals

➢ Bismuth (III) nitrate pentahydrate (Bi $(NO_3)_3 \cdot 5H_2O$), ≥ 99%, Carlo Erbo

➢ Iron (III) nitrate nonahydrate (Fe $(NO_3)_3 \cdot 9H_2O$), 98.0-101.0%, Carlo Erba

➢ Urea ($CH_4N_2O$), Carlo Erba

➢ Potassium hydroxide (KOH), 85%, Carlo Erba

➢ Nitric acid ($HNO_3$), 65% AR grade, Qrec

## 3.2    Sample preparation

The undoped $Bi_2O_2CO_3$ sample was prepared by hydrothermal method. Bi $(NO_3)_3 \cdot 5H_2O$ (0.005 mol), urea (0.05 mol) and 0.1 M nitric acid (20 mL) was mixed and stirred until clear solution is formed. Then, 9 M KOH was dropped into the mixture to adjust the pH to 14. After stirring for 10 min, the mixture was transferred into a Teflon-lined autoclave and heated to 120°C for 13 hours 20 min. Finally, the product was rinsed with distilled water and ethanol, collected by centrifugation and dried at 80°C for overnight. The Fe doped $Bi_2O_2CO_3$ samples were prepared with the same method but Bi $(NO_3)_3 \cdot 5H_2O$ (0.005 - x mol) and Fe $(NO_3)_3 \cdot 9H_2O$ (x = 0, 2.5, 5, 10, 15, 25, 40, 50, 75, 85 and 100 mol%) were used. The name of the sample that can be prepared will be BFxx (xx= mol% Fe doped $Bi_2O_2CO_3$).

BF100 was prepared with the same method, but without the addition of Bi $(NO_3)_3 \cdot 5H_2O$. Only Fe $(NO_3)_3 \cdot 9H_2O$ 100% mol was used in this sample.

## 3.3    Sample characterization

### 3.3.1    X-ray diffractometer (XRD), Model D8 Phaser, Bruker

The samples were ground to powder and put into the sample holder. The powder samples were packed by slide glass for pressure on surface of samples to smooth. X-ray diffraction (XRD) spectra were determined by D8 phaser XRD diffractometer (Bruker) with Cu K$_\alpha$ radiation ($\lambda$ = 1.5406 Å) in 2theta rang of 10-70° by scan rate 0.2 s/step with increment of 0.02°. The phase identification and the crystal structure were identified with the databases by DIFFRACT.EVA program (V 4.2).

### 3.3.2    X-ray photoelectron spectroscopy (XPS), PHI5000 VersaProbe II XPS instruments (ULVAC-PHI, Japan)

This measurement was used to study oxidation state and elemental composition of the samples. X-ray photoelectron spectroscopy was performed by a PHI5000 VersaProbe II XPS instruments (ULVAC-PHI, Japan) (Monochromatic X-ray of Al K$_\alpha$ = 1486.6 eV) at Thailand Center of Excellence in Physics (ThEP), Chiang Mai, Thailand. The binding energy of C1s at 284.8 eV was used as a reference.

### 3.3.3    Transmission Electron Microscopy (TEM), JEOL2100plus

Field-emission transmission electron microscope (FETEM) using high accelerating voltage at 300 kV was used to reveal the morphologies and elemental composition of the samples.

### 3.3.4    Scanning Electron Microscopy (SEM)/Energy Dispersive X-ray Spectroscopy (EDS), Zeiss AURIGA

In the experiment, the samples were prepared on a layer of aluminum (Al) without carbon because the samples have carbon content. The SEM images were taken by a Zeiss AURIGA Field-emission scanning electron microscope (FE-SEM). Energy dispersive X-ray spectroscopy (EDS) was used for elemental mapping. These techniques yielded morphology, elemental composition, and distribution of particle.

### 3.3.5  Photoluminescence Spectrometer (PL), AvaSpec-2048TEC-USB2-2

The photoluminescence spectra were performed by AvaSpec-2048TEC-USB2-2 (LED light source 347 nm, FWHM 15nm, 20 microwatts) at Thailand Center of Excellence in Physics (ThEP), Chiang Mai, Thailand.

### 3.3.6  Diffused reflectance spectroscopy (DRS), UV-Vis-NIR spectrophotometer modeled Carry 5000

UV-Vis-NIR spectrophotometer modeled Carry 5000 was use for optical diffuse reflectance spectroscopy (DRS). The diffuse reflectance (%R) spectra were recorded in the wavelength range of 200-2000 nm with the double beam mode.

### 3.3.7  $N_2$ adsorption-desorption, Bel-Japan Bel Sorp mini II

The specific surface area was determined by physical adsorption of the unreactive $N_2$ gas on solid surface. increasing reactive pressure that more gas molecules had adsorbed on the surface and cover the entire. The nmber of gas molecules is recorded from the volume adsorbed and used to determine the area of the accessible surface. The condition of $N_2$ adsorption-desorption was degassed in vacuum at 300°C for 3 h and $N_2$ adsorption is measured at 77 K. The specific surface area was calculated by Brunauer-Emmett-Teller (BET) method.

### 3.3.8  Thermogravimetry/ Differential thermal analysis (TG/DTA), NETZSCH STA449 F3 Simultaneous Thermal Analyzer instrument (STA)

Thermogravimetric analysis (TGA) was used to investigate the decomposition of substances and to find the temperature required to decompose all organic species in the samples prepared by hydrothermal method in order to determine the calcining temperature. Thermal decomposition of sample was investigated by TG/DTA using a NETZSCH STA449 F3 Simultaneous Thermal Analyzer instrument (STA). The powder of sample was put in 1/2 of $Al_2O_3$ crucible (10-20 g) and heat under the following condition: $N_2$ gas flow (100mL/min); heat rate of 10°C min$^{-1}$; and temperature range of 35-600°C.

## 3.4 Photocatalytic test
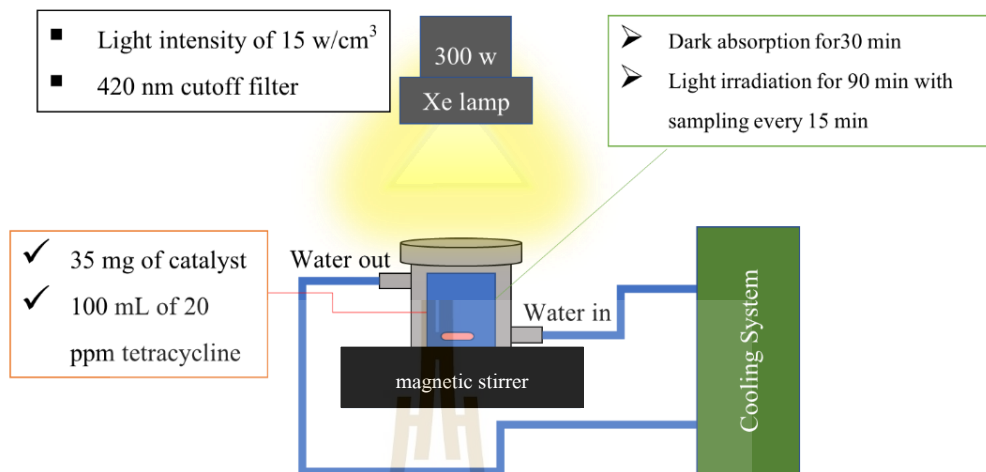


**Figure 3.1** Schematic diagrams of photocatalytic test.

The photocatalytic activities were evaluated by photodegradation of tetracycline as an organic pollutants model. The photocatalysts (35 mg) were put into tetracycline solution (20 ppm,100 mL) under magnetic stirring. The mixture was stirred in the dark for 30 min and subject to light irradiation for 3 hours using Xe-lamp (300 W). The degradation of tetracycline was determined by the intensity of absorption peak of tetracycline (357 nm) as measured by a UV-Vis spectrophotometer.

# CHAPTER IV

# RESULT AND DISCUSSION

## 4.1 Crystal structure, morphology, and BET surface area

Phase identification of undoped $Bi_2O_2CO_3$ and Fe-doped $Bi_2O_2CO_3$ were studied by XRD technique. Figure 4.1 show XRD patterns of all prepared samples. All diffraction peaks can be indexed as the orthorhombic $Bi_2O_2CO_3$ crystal structure (ICSD #94740) with I$mm$2 space group (Huang et al., 2014). Comparing undoped $Bi_2O_2CO_3$ and 75 mol% Fe-doped $Bi_2O_2CO_3$, the peak positions were not changed significantly. However, the peak intensities of (002) and (103) plane obviously varies from sample to sample. However, we were chosen five main samples for study characterization such as BF00, BF05, BF15, BF40 and BF75 as shown Figure 4.2.
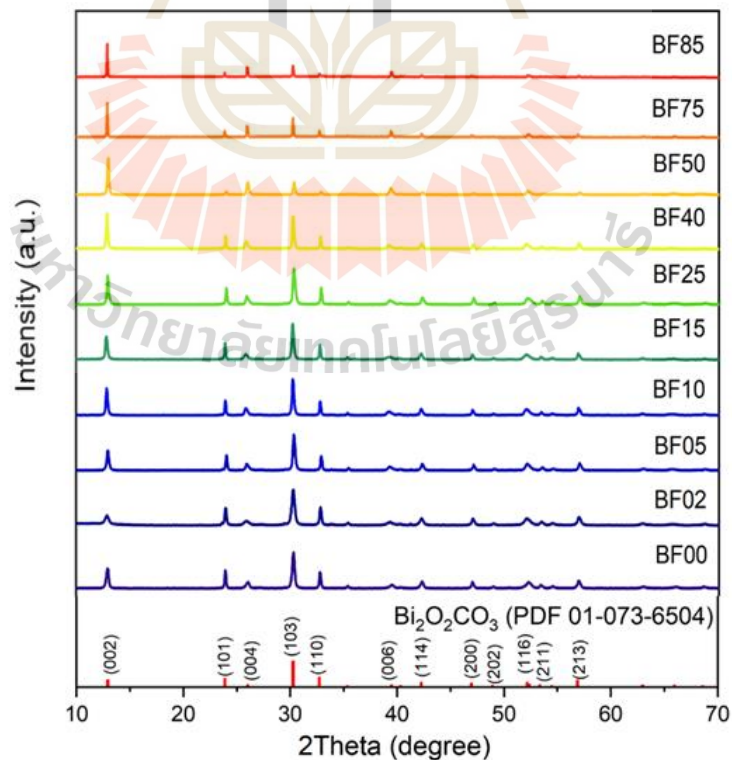


**Figure 4.1** XRD patterns of pristine and Fe-doped $Bi_2O_2CO_3$ samples.
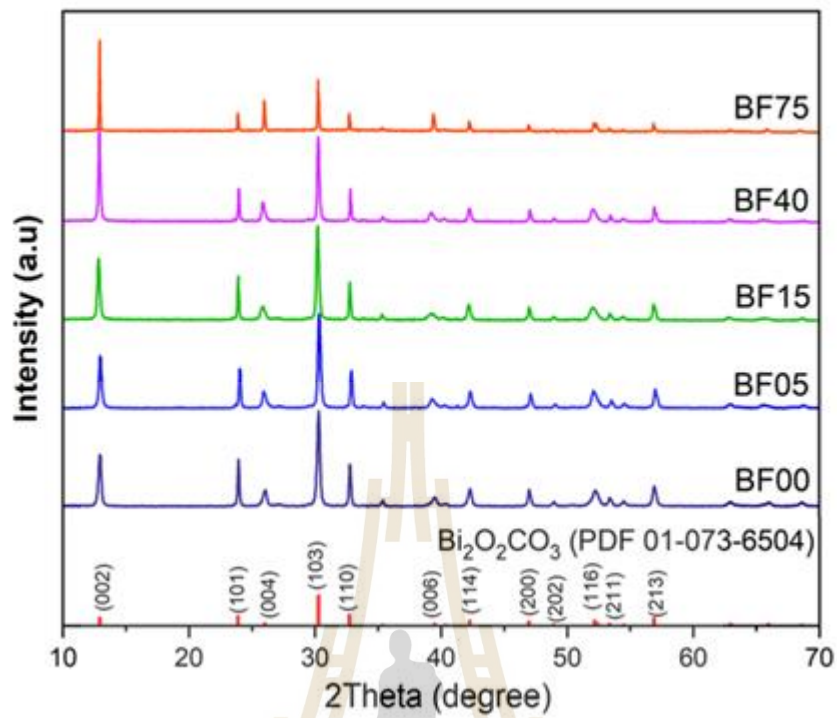
**Figure 4.2** XRD patterns of 5 main samples for study.
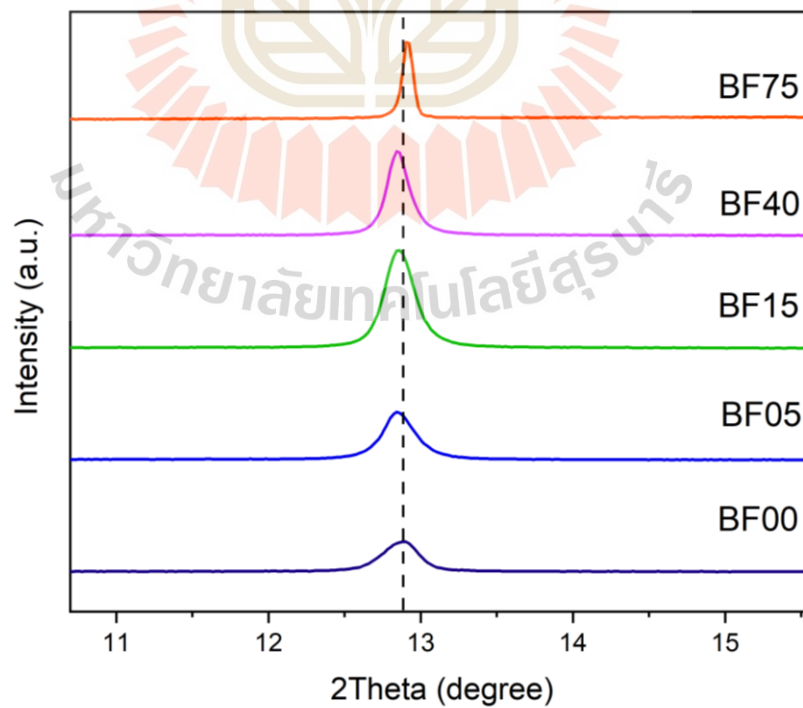


**Figure 4.3** Shifting XRD peak of pristine and Fe-doped $Bi_2O_2CO_3$ samples.
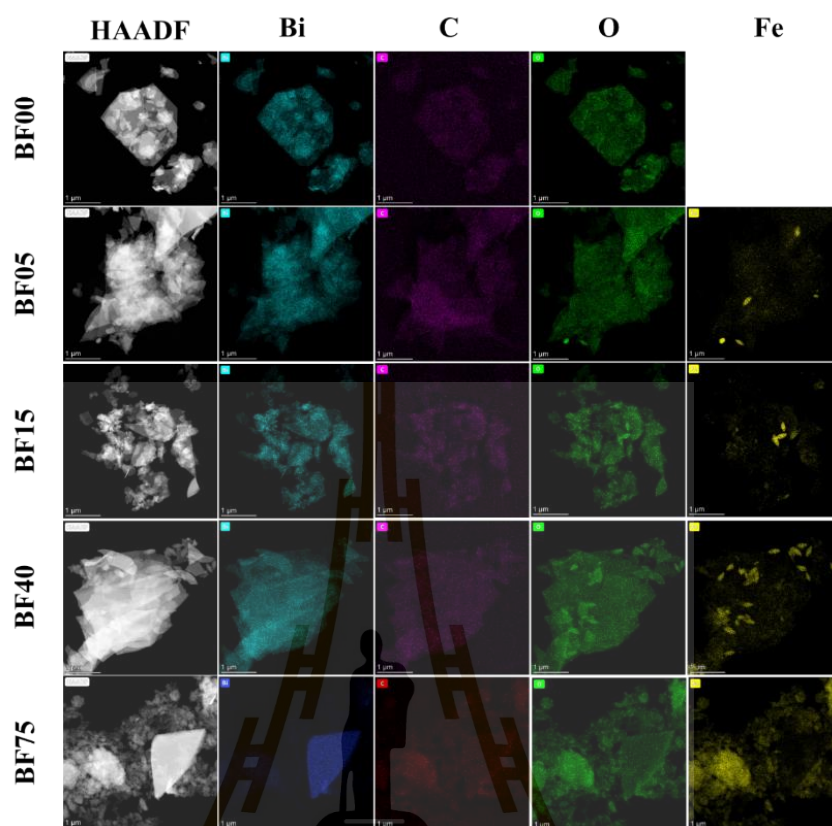
**Figure 4.4** EDS elemental mapping of the sample.

**Table 4.1** $I_{(002)}/I_{(103)}$ ratio, Bi:Fe mol ratio and BET surface area of the samples.

| Sample name | $I_{(002)}/I_{(103)}$ | Bi:Fe mole ratio (average from EDS) | | BET Surface area (m²/g) |
|---|---|---|---|---|
| | | Bi | Fe | |
| BF00 | 0.53 | 2 | - | 1.5 |
| BF05 | 0.55 | 1.59 | 0.39 | 2.8 |
| BF15 | 0.64 | 1.52 | 0.52 | 3.3 |
| BF40 | 1.09 | 1.02 | 1 | 3.4 |
| BF75 | 1.82 | 0.44 | 1.49 | 24.2 |

The energy-dispersive X-ray spectroscopy (EDS) mapping of BF05, BF15, BF40 and BF75 were used to study the elemental composition. As show in Figure 4.4, the presence of Bi, C, O and Fe element in Fe doped $Bi_2O_2CO_3$ samples is confirmed. Moreover, the increased Fe content is detected in Fe doped $Bi_2O_2CO_3$, which coincide with the nominal composition (Table 4.1). As shown Figure 4.3, the diffraction peaks at 12.9° of all prepared samples shifted, with BF05, BF15 and BF40 shifting to the lower degree and BF75 shifting to the higher degree. The cell parameters of the samples decrease upon Fe incorporation in the $Bi_2O_2CO_3$ lattice although $Fe^{3+}$ is smaller than $Bi^{3+}$ (Shannon, 1976; Shannon and Prewitt, 1969). However, the layered structure of $Bi_2O_2CO_3$ could accommodate the interlayered $CO_3^{2-}$ ion, which would result in an increased cell parameter and a shift of the diffraction peaks to lower degrees (Huang, H., Li, X. et al., 2015). The presence of extra $CO_3^{2-}$ ion in the structure was analyzed by thermogravimetric analysis (TGA) technique. TGA curves of undoped $Bi_2O_2CO_3$ and Fe doped $Bi_2O_2CO_3$ samples are shown in Figure 4.5, which exhibits weight loss in the temperature range of 250-400 °C. The weight loss of BF00, BF05, BF15, BF40 and BF75 are 10%, 11.94%, 12.76%, 11.2% and 12.21%, respectively. It is noted that $CO_3^{2-}$ content in the pristine $Bi_2O_2CO_3$ is approximately 8.6%, and the higher weight loss represents extra $CO_3^{2-}$ ion (Huang, H., Li, X. et al., 2015). The observed higher weight loss suggests that our samples contain interlayered $CO_3^{2-}$. The presence of interlayered $CO_3^{2-}$ can be rationalized by our preparation method which includes addition of excess urea. It is important to perceive that optimum carbonate doping in $Bi_2O_2CO_3$ could improve visible light absorption and benefit the photocatalytic performance (Boxall et al., 2003).
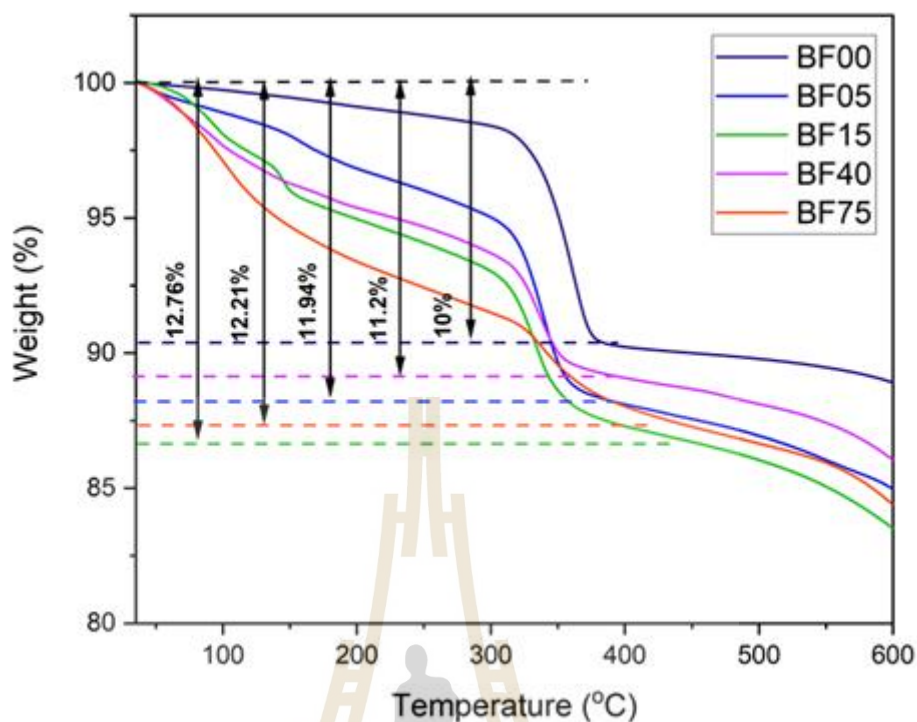
**Figure 4.5** TGA curves of undoped $Bi_2O_2CO_3$ and Fe doped $Bi_2O_2CO_3$ samples.

The scanning electron microscope (Figure 4.6) and the transmission electron microscope (Figure 4.7) images show the morphology of samples that composed of nanoplates with smooth surface. The sizes of the nanoplates are varied from around 1 to 10 μm with similar thickness. While the average elemental composition and Fe content in each sample agree quite well with the starting Fe: Bi ratio (Table 4.1), elemental mapping clearly indicates mixed phases in the samples. The Fe-rich phase forms smaller particles on top of the $Bi_2O_2CO_3$ (Figure 4.2). The formation of impurity phase indicates that solubility of Fe in $Bi_2O_2CO_3$ structure is limited. Moreover, when Fe content is increased to 100% (correspond to $Fe_2O_2CO_3$ composition), $Fe_2O_3$ were obtained as a major phase with lower diffraction intensity of FeO(OH) and no trace of $Bi_2O_2CO_3$ phase (Figure 4.8). Nevertheless, it is noted that Fe is also distributed in the plates as well. Therefore, we conclude that some of the added Fe are included in the $Bi_2O_2CO_3$ lattice while the rest form separate phases with high Fe content, which could also explain an unclear trend in the shift of the XRD patterns upon Fe addition. Since no other elements are detected, this Fe-rich phase is most probably Fe oxides such

as $Fe_2O_3$, FeOOH, FeO, and $Fe_3O_4$. Similar forms of Fe oxides are often referred to as $FeO_x$ for simplicity (Cheng et al., 2016; Liu et al., 2022; Saada et al., 2019). Note that these impurity phases are not detected in the XRD patterns. The reasons for their absence are the low $FeO_x$ crystallinity (Liu et al., 2022; Wang et al., 2019; Zhao et al., 2013) and lower X-ray scattering power of $FeO_x$ comparing to $Bi_2O_2CO_3$. Moreover, we checked the XRD pattern of $Fe_2O_3$ and $Bi_2O_2CO_3$ mixture with several weight ratios and found that intensity of $Fe_2O_3$ diffractions is much lower, even though crystalline $Fe_2O_3$ was used (Figure 4.9). Thus, the $FeO_x$ diffractions in XRD patterns of the samples is not easily detected in the presence of $Bi_2O_2CO_3$.

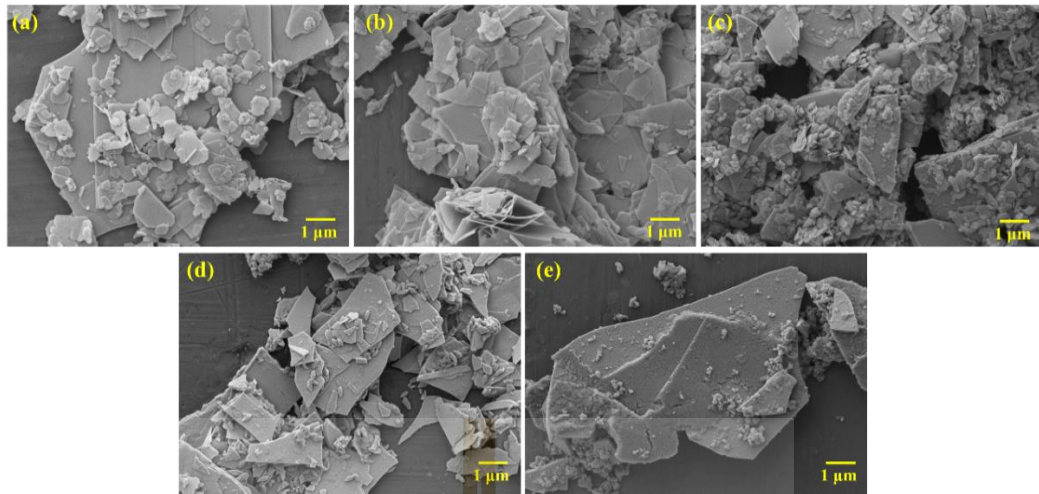**Figure 4.6** SEM image of BF00 (a), BF05 (b), BF15 (c), BF40 (d), and BF75 (e).
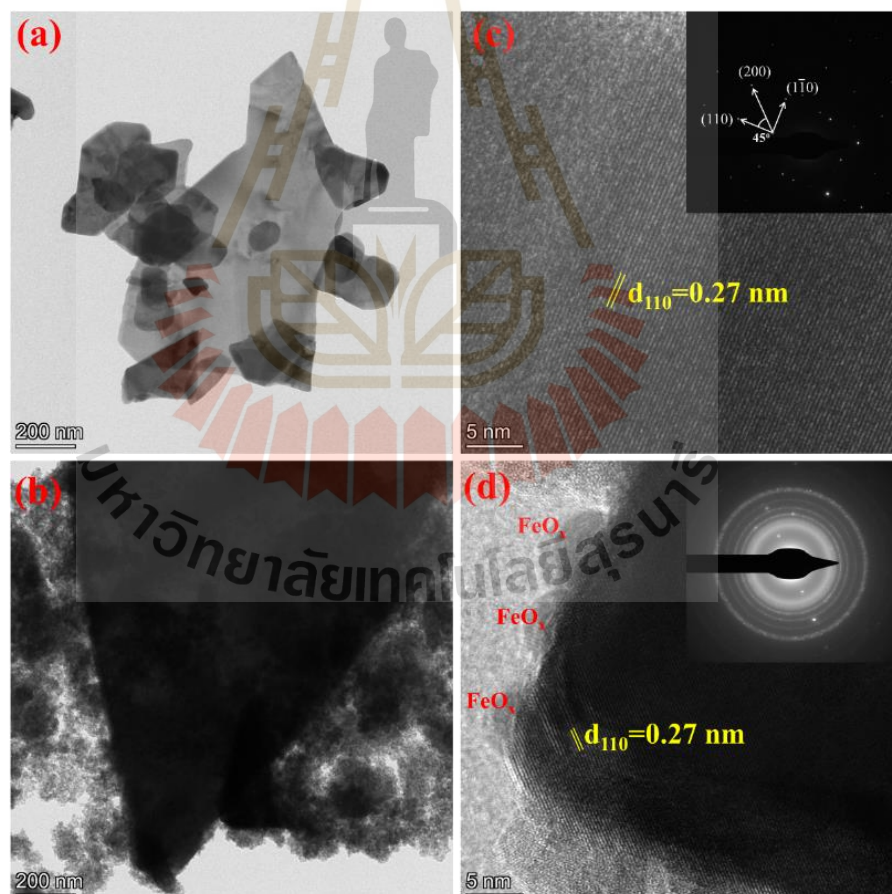


**Figure 4.7** TEM and HRTEM images of BF00 (a and c) and BF75 (b and d) and SAED
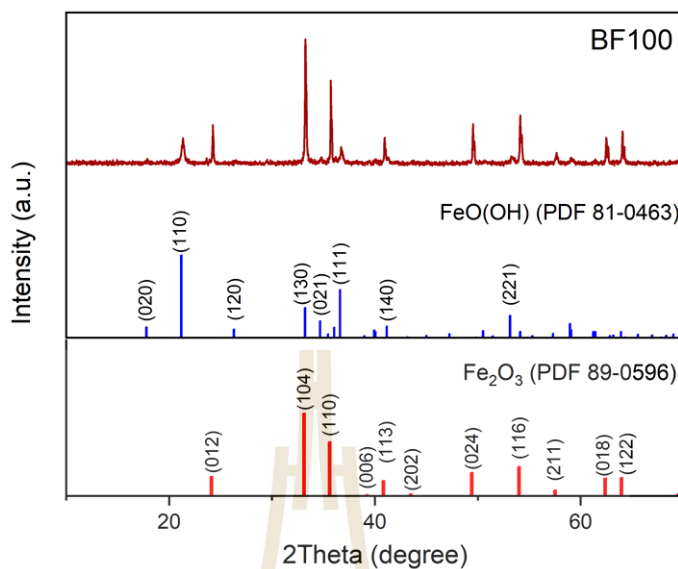patterns of BF00 (inset a) and BF75 (inset d).

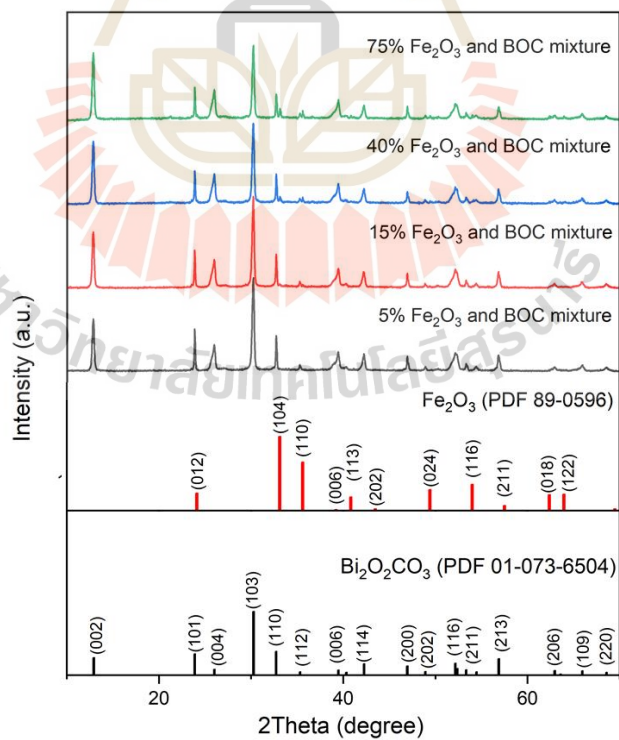**Figure 4.8** XRD pattern of BF100, where Fe content is 100 mol%.



**Figure 4.9** XRD patterns of the $Fe_2O_3$ and $Bi_2O_2CO_3$ mixtures with different weight ratios, including 5, 15, 40 and 75 mol%.

Although the XRD pattern seems unchanged, the higher (002) and (004) intensity in Fe incorporated samples comparing to pure $Bi_2O_2CO_3$ indicates that adding Fe results in a preferred growth of {002} facets (Yang et al., 2016). To clearly compare the preferred growth, we calculate the intensity ratio of (002)/(103) diffraction ($I_{(002)}/I_{(103)}$) for each sample as summarized in Table 4.1. The increase in $I_{(002)}/I_{(103)}$ shows strong correlation with Fe content. {001} facets of $Bi_2O_2CO_3$ are active for photocatalytic reactions due to the increased carrier's separation (Ding et al., 2020; Huang, H., Li, X. et al., 2015), thus the Fe added samples are expected to show good activities.

The morphologies and exposed facets of the samples are also check with the high-resolution TEM (HRTEM). TEM images (Figure 4.7(a) and (b)) confirm the plate-like features of the samples. From Figure 4.5(c), BF00 shows obvious lattice fringes with lattice spacing of 0.27 nm, which is assigned to the (110) crystal planes of $Bi_2O_2CO_3$ (Huang H. et al., 2015; Xu et al., 2017). Selected-area electron diffraction (SAED) analyses also show that BF00 has high crystallinity (Figure 4.7(c)). In addition, the measured angle between (110) and (200) crystallographic planes is 45°, which is consistent the theoretical value. This SAED pattern confirms that BF00 has (002) exposed facet (Xu et al., 2017). The HRTEM image of BF75 is shown in Figure 4.6(d). The inter-planar distance obtained are close to the (110) crystal planes of $Bi_2O_2CO_3$. SAED of BF75 displays ring patterns, which are characteristic of polycrystalline materials (Figure 4.7d). Although it is difficult to investigate the exposed facet based on SAED, the (002) preferred growth of BF75 is confirmed by the significantly higher XRD intensities of (002), (004) and (006) diffraction as discussed previously. Moreover, HRTEM image of BF75 clearly shows the small particles with amorphous nature, which likely correspond to the formed $FeO_x$ (Figure 4.7(d)).

Because of its layered structure, $Bi_2O_2CO_3$ often have preferred growth along (002) facet (Chen et al., 2019; Ding et al., 2020; Yang et al., 2016). In most cases, such orientation is influenced by the synthetic condition such as temperature (Ding et al., 2020) and additives (Cheng et al., 2018). In this work, the only difference between pure $Bi_2O_2CO_3$ and Fe doped $Bi_2O_2CO_3$ is the presence of $Fe^{3+}$ ion. To investigate the origin of different preferred surface orientations in the pure and doped samples, we

calculated and compared the surface energies of pure and 50 mol% Fe-doped $Bi_2O_2CO_3$ (002) surfaces. The surface energies, $\sigma$, are calculated as follow.

$$\sigma = \frac{1}{A}(E_{slab} - nE_{bulk})$$

where $E_{slab}$ is the total energy of the slab model containing $n$ unit cell of bulk structure and $E_{bulk}$ is the total energy of the bulk unit cell. $A$ is the surface area of the slab model. The lower the surface energy, the more preferred surface orientation.

As shown in Figure 4.10(a) and 4.10(b), Bi-terminated surface (002) is the most stable facet for the pure $Bi_2O_2CO_3$ system, while the Fe-terminated surface is most stable for the doped system. Other less stable terminations and their relative energies are included in the Appendix. Computations suggest that Fe-doped $Bi_2O_2CO_3$ prefers the formation of the (002) facet as the surface energy is reduced from 0.134 to 0.045 eV/Å$^2$ upon doping. The calculated results agree with our experimental observations that the XRD peak intensities of (002) plane increases with the doping concentrations.
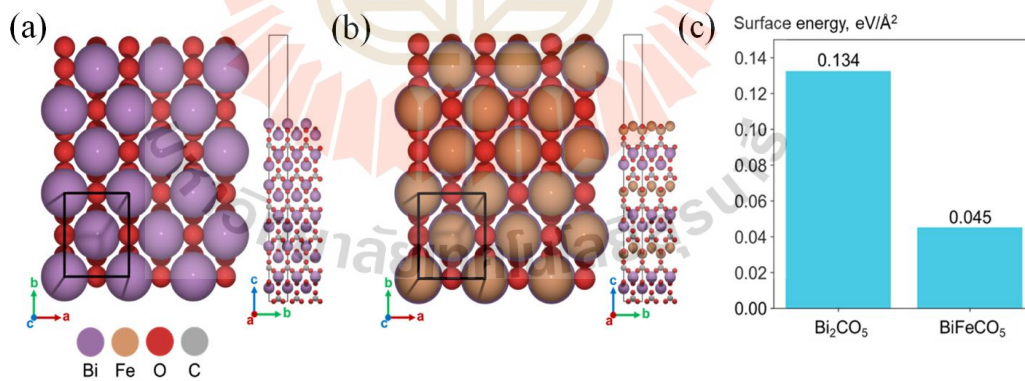


**Figure 4.10** Sketch of surface models used in surface energy calculations for (a) pure and (b) 50 mol% Fe-doped $Bi_2CO_5$ with (c) their corresponding surface energies.

The BET surface areas of all samples are shown in Table 4.1. It was found that the BET surface area of BF00, BF05, BF15, BF40 and BF75 are 1.5 m$^2$/g, 2.8 m$^2$/g, 3.3 m$^2$/g, 3.4 m$^2$/g and 24.2 m$^2$/g , respectively, which is close to those reported in similar

systems (Li et al., 2018). The higher BET surface area might be caused by its thinner plate-like morphology and several small amorphous $FeO_x$ particles deposited on the Fe-doped $Bi_2O_2CO_3$ thin plates.

## 4.2    X-ray photoelectron spectroscopy

X-ray photoelectron spectroscopy (XPS) was used to measure the elemental compositions and to further prove the existence of Fe in Fe doped $Bi_2O_2CO_3$ samples. The C 1s XPS spectra of all samples are shown in Figure 4.11(a). Two strong peaks were observed at around 284.8-285 eV and 287.86-288.46 eV, which can be assigned to hydrocarbon (C-H) and $CO_3^{2-}$ ions in $Bi_2O_2CO_3$, respectively (Li et al., 2018). In addition, the small peak around 284.8-285 eV correspond to adventitious carbon (C-O) (Huang et al., 2014). In Figure 4.11(b), Fe 2p XPS spectra have clear peaks which increase with increasing Fe content, indicating that the Fe doped $Bi_2O_2CO_3$ contain Fe.  Moreover, the high-resolution Fe 2$p$ XPS (Figure 4.9(b)) show two major peaks of Fe 2$p_{3/2}$ and Fe 2$p_{1/2}$, with spin-orbital splitting of about 13.9 eV, and two peaks can be assigned to $Fe^{3+}$. Each major peak can be deconvoluted into two types of Fe bonding, observed at the binding energies 711.2 - 711.4 and 725.0 - 725.2 eV for $Fe^{3+}$ and 709.7 - 709.9 and 723.1 - 723.3 eV for $Fe^{2+}$, which indicates the coexisted oxidation states of $Fe^{3+}$/$Fe^{2+}$ at the surface of Fe added samples (Dutta et al., 2020). It is noted that the binding energies of $Fe^{3+}$ in Fe-added samples are similar to the previously reported values of $Fe^{3+}$ in $Bi_2O_2CO_3$ crystal lattice (Li et al., 2018). $Fe^{2+}$ and parts of $Fe^{3+}$ most likely belong to the $FeO_x$ phase, in agreement with the previously discussed results.

Figure 4.11(c) demonstrate two peaks of Bi 4$f_{7/2}$ and Bi 4$f_{5/2}$ XPS spectra at binding energy of 158.5-158.8 eV and 163.8-164.1 eV, respectively, with spin-orbital splitting of about 5.3 eV, which corresponded to $Bi^{3+}$ ions (Li et al., 2018). By Fe doping, these peaks shifted to lower binding energy, indicating $Bi^{3+}$ ions were reduced by Fe. In case of BF75, two types of Bi bonding were observed at the binding energies at 163.1 and 157.86 eV occurred Bi 4f$_{5/2}$ and Bi 4f$_{7/2}$ of $Bi^{2+}$ state and 164.07 and 158.75 eV occurred Bi 4f$_{5/2}$ and Bi 4f$_{7/2}$ of $Bi^{3+}$ state. The two sets of peaks represent Bi in different environments. Bi in $Bi_2O_2CO_3$ crystal lattice has higher binding energy. On the other hand, oxygen sharing between $Bi_2O_2CO_3$ and $FeO_x$ would lead to electron migration

from Fe to Bi across Fe-O-Bi bond since Fe has lower electronegativity than Bi (Li and Xue, 2006). As a result, Bi at Fe-O-Bi bond would have a lower binding energy. The O 1s XPS spectra of all samples contained three main peaks (Figure 4.11(d)). First, the peaks of around 529.1-529.47 correspond to O bonded with Bi/Fe in the lattice. The second peaks at around 530.1-530.5 eV can be assigned to C in the lattice and adventitious C such as C-O and C=O (Huang et al., 2014). And, the third peaks of around 532.2-532.5 eV can be referred to O adsorbed species such as $O_2$ and $H_2O$ (Jiamprasertboon et al., 2017).
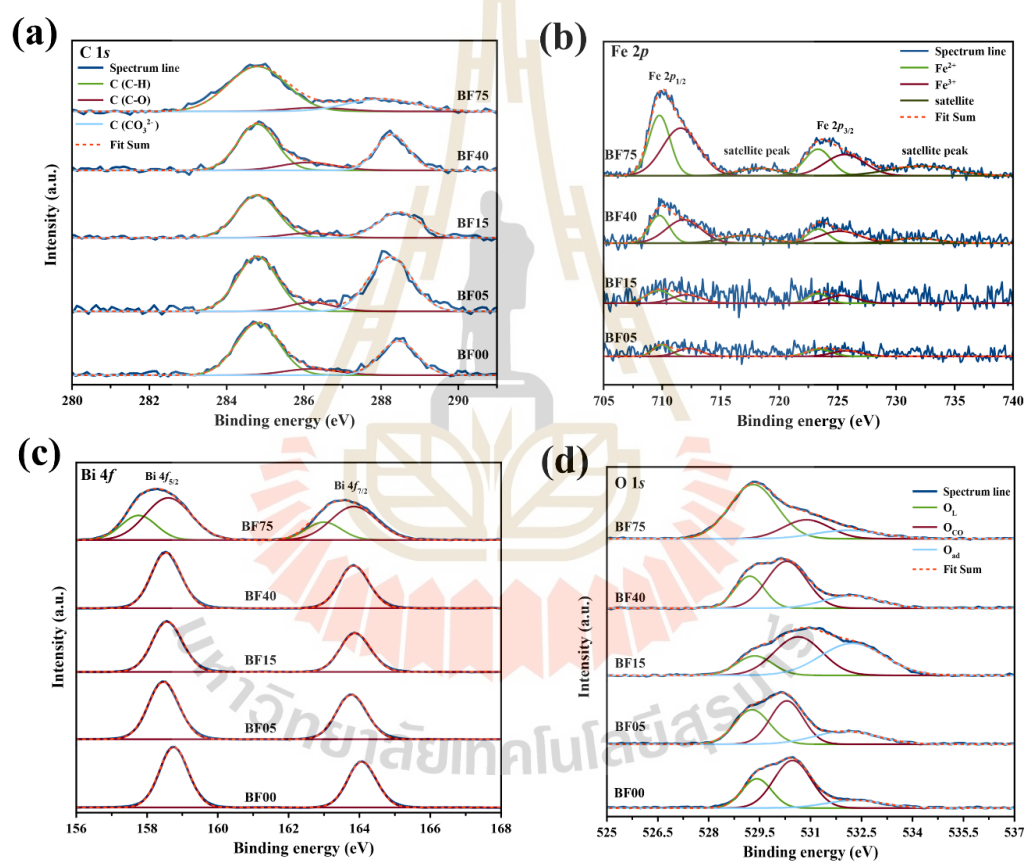


**Figure 4.11** XPS spectra of all samples at core levels of (a) C 1s, (b) Fe 2p, (c) Bi 4f and (d) O 1s.

## 4.3 Optical property and photocatalytic property

The optical properties of $Bi_2O_2CO_3$ and Fe doping samples were characterized by UV-Vis diffused reflectance spectra (UV-vis DRS). As shown in Figure 4.12, $Bi_2O_2CO_3$ has absorption in UV light regions which shifts to visible light regions with increasing amounts of Fe doping. This indicates that Fe doping improves light absorption from UV light to UV-vis light. The red shift in UV-Vis absorption edge of Fe added $Bi_2O_2CO_3$ are caused by both Fe doping which significantly decreases band gap energy of $Bi_2O_2CO_3$ and the presence of $FeO_x$ amorphous (Hu et al., 2014; Li et al., 2018). It is noted that band gap energies of $FeO_x$ phases are about 2 eV (Kurien et al., 2017; Mohanraj and Sivakumar, 2017; Seki, 2018; Sulania et al., 2016; Sultana et al., 2018), which results in the significantly increased light absorption in Fe added samples.
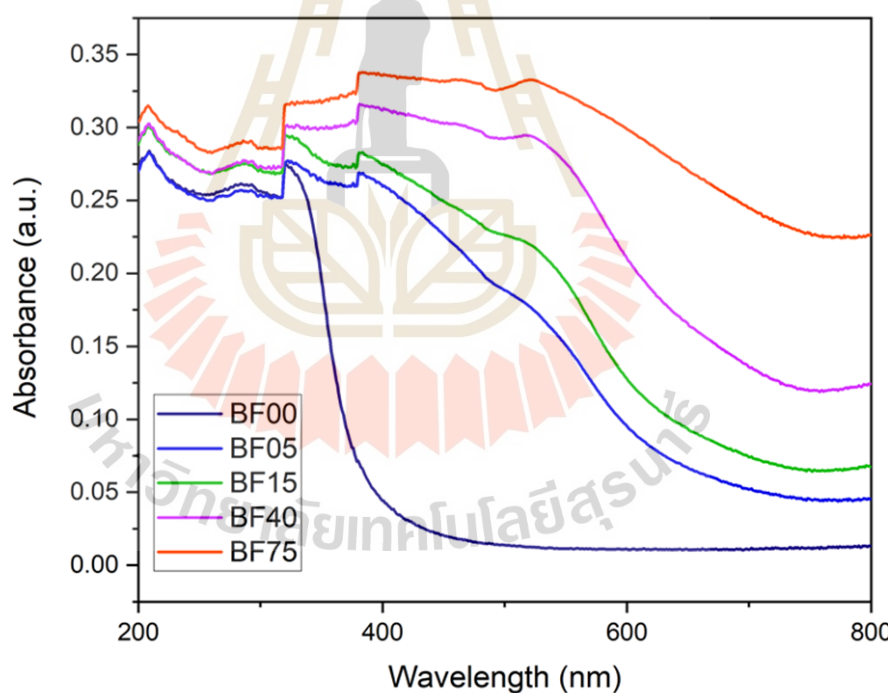


**Figure 4.12** UV-Vis absorption spectra.

The photocatalytic activity of $Bi_2O_2CO_3$ and different Fe-doped $Bi_2O_2CO_3$ samples were evaluated by photodegradation of tetracyclines under visible light irradiation. As shown in Figure 4.1(a), the degradation of tetracycline over BF00, BF05, BF15, BF40 and BF75 are 28%, 31%, 37%, 33% and 62%, respectively. In the case of BF85, the photodegradation of TC had degraded as well as BF75, while the

photodegradation activity of BF100 had decrease (Figure 4.13(b)), indicating that the photodegradation activity of Fe doped $Bi_2O_2CO_3$ was limited at 75 mol% Fe content.
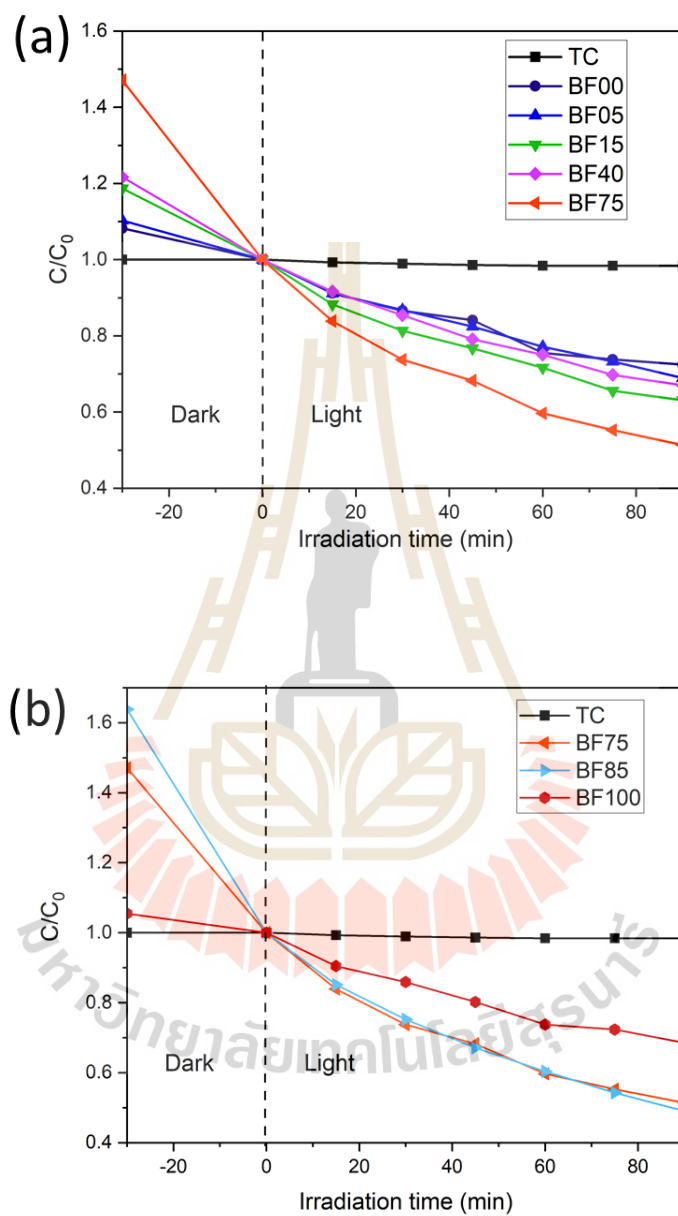


**Figure 4.13** The photocatalytic activity of tetracycline degradation of 5 main samples (a) BF85 and BF100 (b).

Thus, 75mol% Fe addition can improve photocatalytic activity of $Bi_2O_2CO_3$ and shows the highest photocatalytic activity with TC photodegradation at 62%, which is about 2.2 times of activity of the pristine $Bi_2O_2CO_3$ (BF00). The photodegradation rate is also investigated by the pseudo first order kinetics using the equation.

$$ln(C_0/C_t) = k_{app}t$$

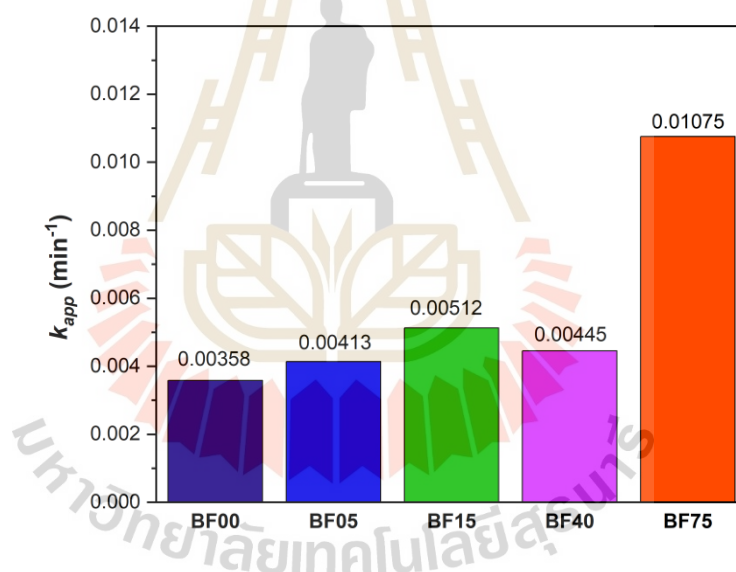where $C_0$ is initial tetracycline concentration (mg/L), $C_t$ is tetracycline concentration at time t, (mg/L), and $k_{app}$ is the rate constant of apparent pseudo first order reaction ($min^{-1}$). As summarized in Figure 4.14, BF75 has the highest rate constant of about 0.011 $min^{-1}$, which is almost three times higher than that of the pristine $Bi_2O_2CO_3$.



**Figure 4.14** The rate constants of apparent pseudo first order reaction.

It is well known that photocatalytic activity is directly related with several factors. The most obvious factor in this work is the reduction in band gap energy. The high light absorption of BF75 increases its ability to generate electron-hole pairs and consequently improves the photocatalytic activity. In addition, the adsorption capacity of tetracycline molecules on the catalysts surface also influences the photocatalytic

performance. In the dark (Figure 4.13(a), light off range), BF75 also shows the highest adsorption, which improves that the degradation efficiency. Moreover, separation and migration of photogenerated carriers are also crucial factors in photocatalysis. We use photoluminescence (PL) measurement to investigate the electron–hole pair recombination.

In the general, photoluminescence (PL) spectra are study the efficiency of charge carrier trapping, transfer and recombination degree of the photogeneration electrons and holes (Tian et al., 2013). PL intensity probes separation efficiency of electron-hole pairs, the low PL intensity means high separation efficiency of electron-hole pairs (Álvarez et al., 2019; Huang et al., 2015). As shown in Figure 4.15, the Fe-doped $Bi_2O_2CO_3$ samples show lower PL intensity comparing to BF00 sample, which suggests that the Fe-doped $Bi_2O_2CO_3$ samples have improved separation efficiency of charge carriers. Obviously, the BF75 demonstrates the highest separation efficiency of charge carriers.
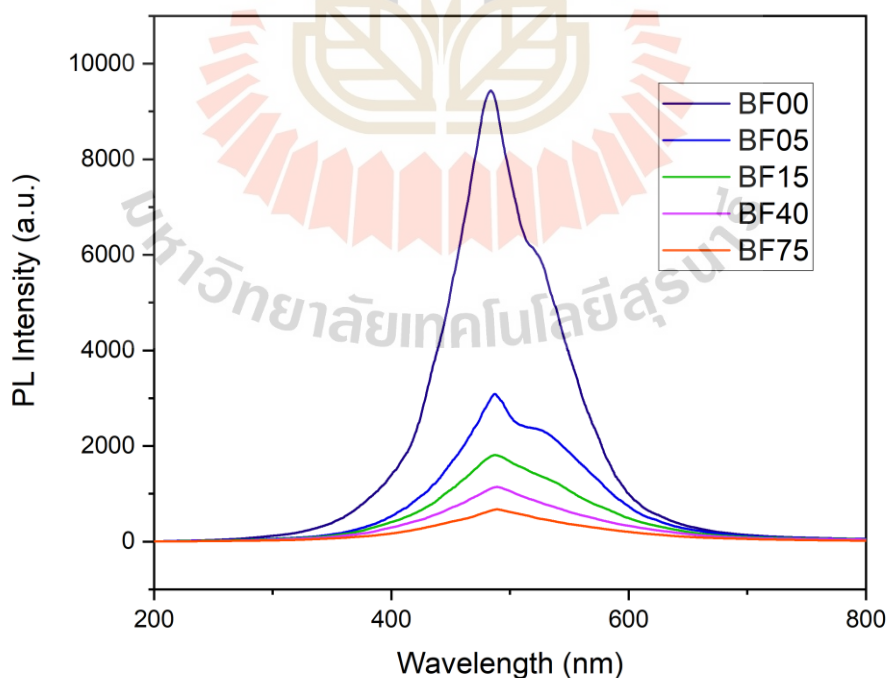


**Figure 4.15** The photoluminescence properties of the samples.

Interestingly, it was previously concluded that high Fe content in the lattice results in a decreased activity as Fe could act as recombination centers (Li et al., 2018). In this work, we see the continued improvement of carrier separation even in samples with high Fe content. Thus, $FeO_x$ phase must have additional roles in reducing carrier recombination here. $FeO_x$ is often used as a cocatalyst in photocatalysis. The catalysts modified with $FeO_x$ display more light absorption ability and more charge carrier generation, leading to higher efficiencies (Liu et al., 2022; Sołtys-Mroz et al., 2021).

In order to understand the photocatalytic mechanism of $FeO_x/Fe\text{-}Bi_2O_2CO_3$, isopropanol (IPA), sodium oxalate ($Na_2C_2O_4$), and benzoquinone (BQ) were used as hydroxyl radical (•OH), hole ($h^+$) and superoxide radical ($O_2^{\bullet-}$) scavengers, respectively (Zhang et al., 2016). The inhibition of tetracycline photocatalytic degradation over BF75 in the presence of different scavengers is shown in Figure 4.16. The percentages of inhibition after 90 min are 2.07%, 11.28%, and 41.19% when IPA, $Na_2C_2O_4$ and BQ are added, respectively. This result indicated that superoxide radical ($O_2^{\bullet-}$) is the main active species for tetracycline photodegradation over BF75 under visible light irradiation. On the other hand, photoexcited hole ($h^+$) and hydroxyl radicals (•OH) are the minor active species in this process.
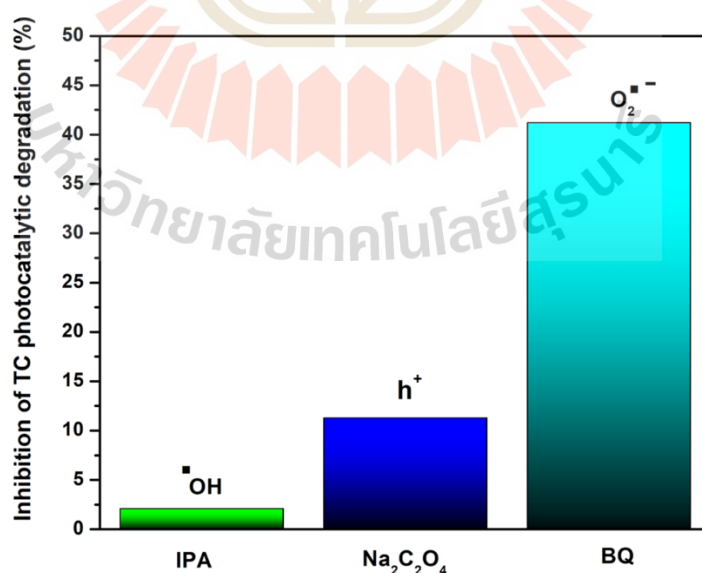


**Figure 4.16** The inhibition of tetracycline photocatalytic degradation over BF75 in the presence of different scavengers under visible light irradiation.

This result is interesting because the previous reports have shown that the main active species in dye degradation of $Bi_2O_2CO_3$ with {001} exposed facet is holes, not superoxide radical (Yang et al., 2016; Yang et al., 2020; Zhang et al., 2016). The different active species as obtained here indicate that $FeO_x$ plays some roles in altering the active species generation and hence the photocatalytic degradation mechanism. The photocatalytic mechanism of $FeO_x/Fe-Bi_2O_2CO_3$ is proposed as summarized in Figure 4.17. Adding Fe both replaces parts of Bi in the lattice and forms amorphous $FeO_x$ as co-catalysts, which cause a red shift on the optical absorption edge. Under visible light irradiation, the conduction and valence bands of Fe-doped $Bi_2O_2CO_3$ create more photoexcited electrons-holes pairs. $FeO_x$ containing Fe (III) act as a cocatalyst which traps the photogenerated electrons and reduces carrier recombination as proven from the significantly lower PL intensity in $Fe-Bi_2O_2CO_3$ samples (Cheng et al., 2016; Liu et al., 2016; Wang et al., 2014). Once Fe(III) traps electrons, it is reduced to Fe(II), which then generates $O_2^{\bullet-}$ (the redox potential of $O_2/O_2^{\bullet-}$ (−0.13 V vs NHE)) and changes back to $Fe^{3+}$ (Li et al., 2022; McBain, 1901). As a result, more oxidizing radicals are generated and can participate in tetracycline degradation. Moreover, electrons in the valence band of Fe doped $Bi_2O_2CO_3$ can be excited directly to $FeO_x$ through the interfacial charge transfer (IFCT) process (Liu et al., 2016; Qiu et al., 2010; Yu et al., 2010). This process also contributes to the increased light absorption in visible region of the Fe-added samples (Figure 4.12).
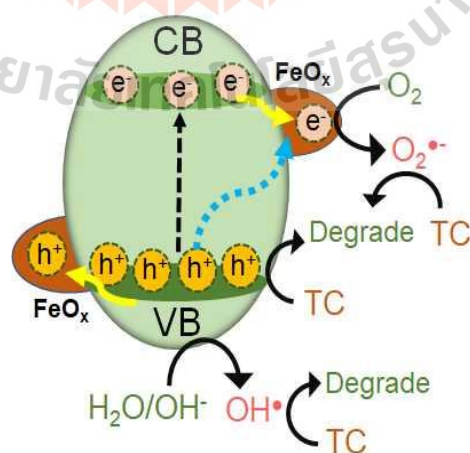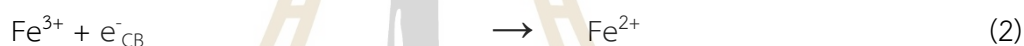


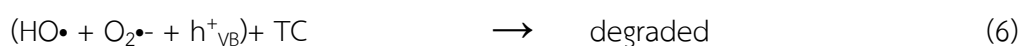**Figure 4.17** A schematic diagram of the photocatalytic mechanism of $FeO_x/Fe-Bi_2O_2CO_3$ system.

Another FeO$_x$ phase containing Fe (II) might also act as hole trapping centers (Rao et al., 2017; Shoneye and Tang, 2020). Holes are created in the valence band of Fe-Bi$_2$O$_2$CO$_3$ and transfer to FeO$_x$ phase which oxidize Fe (II) to Fe (III), which further benefits the electrons-holes separation. However, Fe$^{3+}$/Fe$^{2+}$ cycle reduce the formation of OH• and holes (h$^+$) as the redox potential of Fe$^{3+}$/Fe$^{2+}$ (+0.77 V vs NHE) is less negative than those of H$_2$O/ OH• (+2.73 V vs NHE) and OH$^-$/OH• (+1.99 V vs NHE) (Ding et al., 2021; Li et al., 2022). As a result, both OH• and h$^+$ are only minor active species in this work. Note that the small quantity of OH• and h$^+$ as shown in Figure 4.10a could be created *via* valence band without going through FeO$_x$ nanocluster. In summary, the process of tetracycline photodegradation by the coupling system of FeO$_x$/Fe-Bi$_2$O$_2$CO$_3$ is as follows:

$$\text{FeO}_x/\text{Fe-Bi}_2\text{O}_2\text{CO}_3 + h\textbf{V} \text{ (Visible)} \longrightarrow \text{FeO}_x/\text{Fe-Bi}_2\text{O}_2\text{CO}_3 \ (e^-_{CB} + h^+_{VB}) \quad (1)$$

○ Conduction band

$$\text{Fe}^{3+} + e^-_{CB} \longrightarrow \text{Fe}^{2+} \quad (2)$$

$$\text{Fe}^{2+} + \text{O}_2 \longrightarrow \text{O}_2^{•-} + \text{Fe}^{3+} \quad (3)$$

○ Valence band

$$e^-_{VB} + \text{Fe}^{3+} \longrightarrow \text{Fe}^{2+}$$

$$h^+_{VB} + \text{Fe}^{2+} \longrightarrow \text{Fe}^{3+} \quad (4)$$

$$h^+_{VB} + \text{H}_2\text{O/OH}^- \longrightarrow \text{OH}• \quad (5)$$

$$(\text{HO}• + \text{O}_2•- + h^+_{VB}) + \text{TC} \longrightarrow \text{degraded} \quad (6)$$

## 4.4    References

Álvarez, L., Gascue, B. R. d., Tremont, R. J., Márquez, E., and Velazco, E. J. (2019). Synthesis and Characterization of a New Aluminum-Doped Bismuth Subcarbonate. *Crystals, 9*(466), 1-10.

Boxall, A. B. A., Kolpin, D. W., Halling-Sørensen, B., and J. Tolls. (2003). Peer Reviewed: Are Veterinary Medicines Causing Environmental Risks? *Environmental Science & Technology, 37*(15), 286A–294A.

Chen, P., Sun, Y., Liu, H., Zhou, Y., Jiang, G., Lee, S. C., Zhang, Y., and Dong, F. (2019). Facet-dependent photocatalytic NO conversion pathways predetermined by adsorption activation patterns†. *Nanoscale, 11*, 2366–2373.

Cheng, L., XuminHu, and Hao, L. (2018). Template-induced $Bi_2O_2CO_3$ microstructure selfassembled by nanosheets with exposed {001} facets. *Materials Research Express, 5*, 065901.

Cheng, R., Zhang, L., Fan, X., Wang, M., Li, M., and Shi, J. (2016). One-step construction of $FeO_x$ modified $g$-$C_3N_4$ for largely enhanced visible-light photocatalytic hydrogen evolution. *Carbon, 101*, 62-70.

Ding, C., Chen, L., Ni, Z., Chen, Z., Li, J., Chen, L., Su, F., and Huang, Y. (2021). Fluorescent Nanoscale Covalent Organic Frameworks with the Theoretically Matched Redox Potential of $Fe^{3+}$/$Fe^{2+}$ for Monitoring of Adenosine-5′-Triphosphate in Cells. *American Chemical Society Applied Nano Materials, 4*, 13132–13139.

Ding, J., Wang, H., Luo, Y., Xu, Y., Liu, J., and Lin, Y. (2020). (002) Oriented $Bi_2O_2CO_3$ Nanosheets with Enhanced Photocatalytic Performance for Toluene Removal in Air. *Catalysts, 10*(389), 1-15.

Dutta, S., Manna, K., Srivastava, S. K., Gupta, A. K., and Yadav, M. K. (2020). Hollow polyaniline Microsphere/ $Fe_3O_4$ nanocomposite as an Effective Adsorbent for Removal of Arsenic from Water. *Scientific Reports, 10*, 4982.

Hu, D., Zhang, K., Yang, Q., Wang, M., Xi, Y., and Hu, C. (2014). Super-high photocatalytic activity of $Fe_2O_3$ nanoparticles anchored on $Bi_2O_2CO_3$ nanosheets with exposed {0 0 1} active facets. *Applied Surface Science 316*, 93–101.

Huang, H., Tian, N., Jin, S., Zhang, Y., and Wang, S. (2014). Syntheses, characterization and nonlinear optical properties of a bismuth subcarbonate $Bi_2O_2CO_3$. *Solid State Sciences, 30*, 1-5.

Huang, Y., Fan, W., Long, B., Li, H., Zhao, F., Liu, Z., Tong, Y., and Ji, H. (2015). Visible light $Bi_2S_3/Bi_2O_3/Bi_2O_2CO_3$ photocatalyst for effective degradation of organic pollutions. *Applied Catalysis B: Environmental, 185*, 68-76.

Jiamprasertboon, A., Kongnok, T., Jungthawan, S., Kidkhunthod, P., Chanlek, N., and Siritanon, T. (2017). Investigation on crystal structures, optical properties, and band structure calculations of $In_{2-x}M_xTeO_6$ *Journal of Alloys and Compounds, 702*, 601-610.

Kurien, U., Hu, Z., Lee, H., Dastoor, A. P., and Ariya, P. A. (2017). Radiation enhanced uptake of $Hg^{0(g)}$ on iron (oxyhydr)oxide nanoparticles. *The Royal Society of Chemistry Advances, 7*, 45010–45021.

Li, J., Liu, Y., Zhou, Y., Liu, S., Liang, Y., Luo, T., and Dai, G. (2018). Enhanced visible-light photocatalytic activity of $Bi_2O_2CO_3$ nanoplates by Fe-doping in the degradation of rhodamine B. *Materials Research Bulletin, 107*, 438-445.

Li, K., and Xue, D. (2006). Estimation of Electronegativity Values of Elements in Different Valence States. *The Journal of Physical Chemistry A, 110*, 11332–11337.

Li, L., Gao, H., Yi, Z., Wang, S., Wu, X., Li, R., and Yang, H. (2022). Comparative investigation on synthesis, morphological tailoring and photocatalytic activities of $Bi_2O_2CO_3$ nanostructures. *Colloids and Surfaces A: Physicochemical and Engineering Aspects, 644*, 128758.

Liu, S., Deng, P., Dai, G., liang, Y., and Zhang, S. (2016). Enhanced photocatalytic performance of hierarchical $Bi_2O_2CO_3$ microflowers by Fe(III) modification. *Ceramics International, 42*, 10094–10098.

Liu, Y., Wang, X., Ye, W., Butenko, D. S., Lu, P., Chen, Q., Cai, R., Sun, J., Zhu, Y., and Yang, D. (2022). $FeO_x$ nanoclusters decorated $TiO_2$ for boosting white LED driven photocatalytic Fenton-like norfloxacin degradation. *Separation and Purification Technology, 303*(122194).

McBain, J. W. (1901). OXIDATION OF FERROUS SOLUTIONS BY FREE OXYGEN. *The Journal of Physical Chemistry A, 5*, 623–638.

Mohanraj, K., and Sivakumar, G. (2017). Synthesis of $\gamma$-Fe$_2$O$_3$, Fe$_3$O$_4$ and Copper Doped Fe$_3$O$_4$ Nanoparticles by Sonochemical Method. *Sains Malaysiana, 46*, 1935-1942.

Qiu, X., Miyauchi, M., Yu, H., Irie, H., and Hashimoto, K. (2010). Visible-Light-Driven Cu(II)-(Sr$_{1-y}$Na$_y$)(Ti$_{1-x}$Mo$_x$)O$_3$ Photocatalysts Based on Conduction Band Control and Surface Ion Modification. *Journal of the American Chemical Society, 132*, 15259–15267.

Rao, G., Zhao, H., Chen, J., Deng, W., Jung, B., Abdel-Wahab, A., and Bill Batchelor, Y. L. (2017). FeOOH and Fe$_2$O$_3$ co-grafted TiO$_2$ photocatalysts for bisphenol a degradation in water. *Catalysis Communications, 97*, 125-129.

Saada, H., Abdallah, R., Fabre, B., Floner, D., Fryars, S., Vacher, A., Dorcet, V., Meriadec, C., Ababou-Girard, S., and Loget, G. (2019). Boosting the performance of BiVO$_4$ prepared by alkaline electrodeposition with an amorphous Fe co-catalyst. *ChemElectroChem, 6*, 613-617.

Seki, M. (2018). Bandgap-Engineered Iron Oxides for Solar Energy Harvesting. *Iron Ores and Iron Oxide Materials*, 255-269.

Shannon, R. D. (1976). Revised Effective Ionic Radii and Systematic Studies of Interatomic Distances in Halides and Chalcogenides. *Acta crystallographica section A: crystal physics, diffraction, theoretical and general crystallography, 32*, 751-767.

Shannon, R. T., and Prewitt, C. T. (1969). Effective ionic radii in oxides and fluorides. *Acta Crystallographica Section B: Structural Crystallography and Crystal Chemistry, 25*, 925-946.

Shoneye, A., and Tang, J. (2020). Highly dispersed FeOOH to enhance photocatalytic activity of TiO$_2$ for complete mineralisation of herbicides. *Applied Surface Science, 511*, 145479.

Sołtys-Mróz, M., Syrek, K., Wiercigroch, E., Małek, K., Rokosz, K., Raaen, S., and Sulka, G. D. (2021). Enhanced visible light photoelectrochemical water splitting using nanotubular FeO$_x$-TiO$_2$ annealed at different temperatures. *Journal of Power Sources, 507*.

Sulania, I., Kaswan, J., Attatappa, V., Karn, R. K., Agarwal, D. C., and Kanjilal, D. (2016). Investigations of electrical and optical properties of low energy ion irradiated $\alpha$–$Fe_2O_3$ (hematite) thin films. *Journal of Applied Physics, 1731*.

Sultana, S., Mansingh, S., and Parida, K. (2018). Rational design of light induced self healed Fe based oxygen vacancy rich $CeO_2$ ($CeO_2NS$–$FeOOH$/$Fe_2O_3$) nanostructure materials for photocatalytic water oxidation and Cr(vi) reduction. *Journal of Materials Chemistry A 6*, 11377-11389.

Tian, J., Sang, Y., Zhao, Z., Zhou, W., Wang, D., Kang, X., Liu, H., Wang, J., Chen, S., Cai, H., and Huang, H. (2013). Enhanced Photocatalytic Performances of $CeO_2$ /$TiO_2$ Nanobelt Heterostructures. *Small, 22*, 3864-3872.

Wang, X., Wang, K., Feng, K., Chen, F., Yu, H., and Yu, J. (2014). Greatly enhanced photocatalytic activity of $TiO_{2-x}N_x$ by a simple surface modification of Fe(III) cocatalyst. *Journal of Molecular Catalysis A: Chemical, 391*, 92–98.

Wang, Y., Cao, X., Hu, Q., Liang, X., Tian, T., Lin, J., Yue, M., and Ding, Y. (2019). $FeO_x$ Derived from an Iron-Containing Polyoxometalate Boosting the Photocatalytic Water Oxidation Activity of $Ti^{3+}$-Doped $TiO_2$. *American Chemical Society Applied Materials & Interfaces, 11*, 3135–23143.

Xu, J., Wang, K. K., Liu, T., Peng, Y., and Xu, B. G. (2017). Br-doped $Bi_2O_2CO_3$ exposed (001) crystal facets with enhanced photocatalytic activity. *CrystEngComm, 19*, 5001-5007.

Yang, L.-M., Zhang, G.-Y., Wang, H.-R., Bai, X., Shen, X.-Q., Liu, J.-W., and Gao, D.-Z. (2016). Mild synthesis of {001} facets predominated $Bi_2O_2CO_3$ clusters with outstanding simulated sunlight photocatalytic activities. *CrystEngComm, 18*, 3683-3695.

Yang, X., Yonglin Wang, He, N., Wan, W., Zhang, F., Zhai, B., and Zhang, P. (2020). One-Step Hydrothermal Synthesis of Hierarchical NanosheetAssembled $Bi_2O_2CO_3$ Microflowers with {001} Dominant Facet and Their Superior Photocatalytic Performance. *Nanotechnology, 31*.

Yu, H., Irie, H., Shimodaira, Y., Hosogi, Y., Kuroda, Y., Miyauchi, M., and Hashimoto, K. (2010). An Efficient Visible-Light-Sensitive Fe(III)-Grafted $TiO_2$ Photocatalyst. *The Journal of Physical Chemistry A, 114*, 16481-16487.

Zhang, Y., Zhu, G., Hojamberdiev, M., Gao, J., Hao, J., Zhou, J., and Liu, P. (2016). Synergistic effect of oxygen vacancy and nitrogen doping on enhancing the photocatalytic activity of $Bi_2O_2CO_3$ nanosheets with exposed {0 0 1} facets for the degradation of organic pollutants. *Applied Surface Science, 371*, 231–241.

Zhao, Z., Dai, H., Deng, J., Liu, Y., Wang, Y., Li, X., Bai, G., Baozu Gao, and Au, C. T. (2013). Porous $FeO_x/BiVO_{4-\delta}S_{0.08}$: Highly efficient photocatalysts for the degradation of Methylene Blue under visible-light illumination. *JOURNAL OF ENVIRONMENTAL SCIENCES, 25*, 2138–2149.

# CHAPTER V

# CONCLUSION

$FeO_x/Fe-Bi_2O_2CO_3$ photocatalysts were successfully prepared *via* a simple hydrothermal method by adding Fe ion during the hydrothermal process. The excess Fe ions form $FeO_x$ nanoparticles while another part of Fe could incorporate into $Bi_2O_2CO_3$ lattice forming $FeO_x/Fe-Bi_2O_2CO_3$ composites. The effects of Fe addition on a preferred orientation and optical property of the samples are significant. Fe in the lattice reduces the surface energy of (002) facet which caused preferred growth of the facet as clearly seen from the increased $I_{(002)}$ in the XRD pattern. As {001} facets enable good carriers' separation, the higher portion of this facets in Fe added samples and Fe doping also increase light absorption to a visible region and thus carriers' generation, which that improved catalytic activity. Moreover, the deposited $FeO_x$ containing both Fe (II) and Fe (III) act as cocatalysts and enhances carrier's generation *via* an interfacial charge transfer. By trapping the generated electron-hole pairs, charge recombination of the catalysts is significantly reduced as confirmed by the much lower PL intensity. Therefore, $FeO_x/Fe-Bi_2O_2CO_3$ with 75 mol% Fe addition exhibit two to three times higher tetracycline degradation efficiency comparing to the pristine $Bi_2O_2CO_3$. Thus, this work has shown that a combination of Fe doping and $FeO_x$ deposition can effectively enhance the photocatalytic activities.

APPENDICES
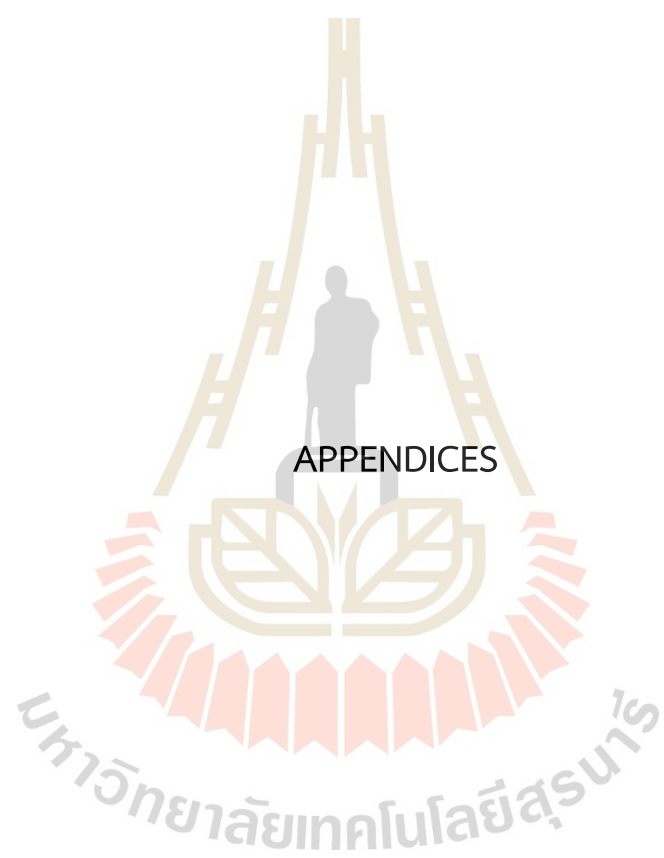
# APPENDIX A

# CALCULATION: BULK AND SURFACE MODELS FOR SURFACE

# ENERGY CALCULATIONS

## 1.    Geometric structure optimization

We optimized the unit cell of $Bi_2O_2CO_3$ as shown in Figure A-1. The optimized $Bi_2O_2CO_3$ structure has lattice constant of 3.61 Å, 4.41 Å and 13.75 Å for a, b and c direction, respectively, containing 4 Bi atoms, 2 C atoms and 10 O atoms.
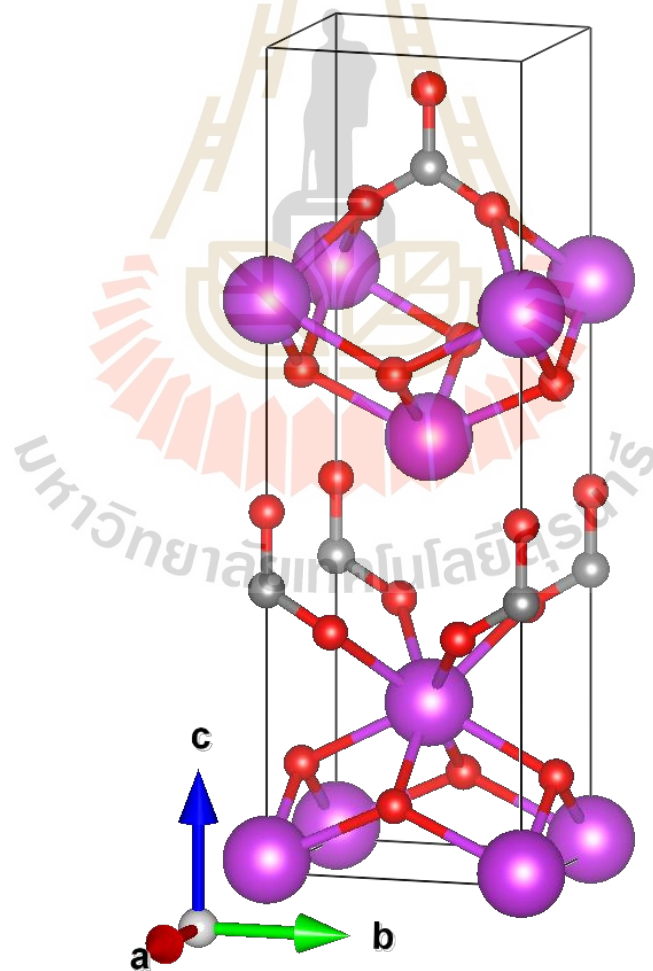


**Figure A-1** The optimized geometric structure of $Bi_2O_2CO_3$. The magenta, red and grey sphere represent Bi, O and C atom, respectively.

For BiFeO$_2$CO$_3$, we varied position of 2 Fe atoms substitute that of Bi atoms in Bi$_2$O$_2$CO$_3$ structure. Six configurations of BiFeO$_2$CO$_3$, as shown in Figure A-2, was consider. The most stable of BiFeO$_2$CO$_3$ configuration is config2 and config5, as shown in relative energy plot in Figure A-3. The config2 and config5 of BiFeO$_2$CO$_3$ structure show alternating layers between BiO, FeO and CO$_3$ layers.



config1    config2    config3     config4    config5    config6
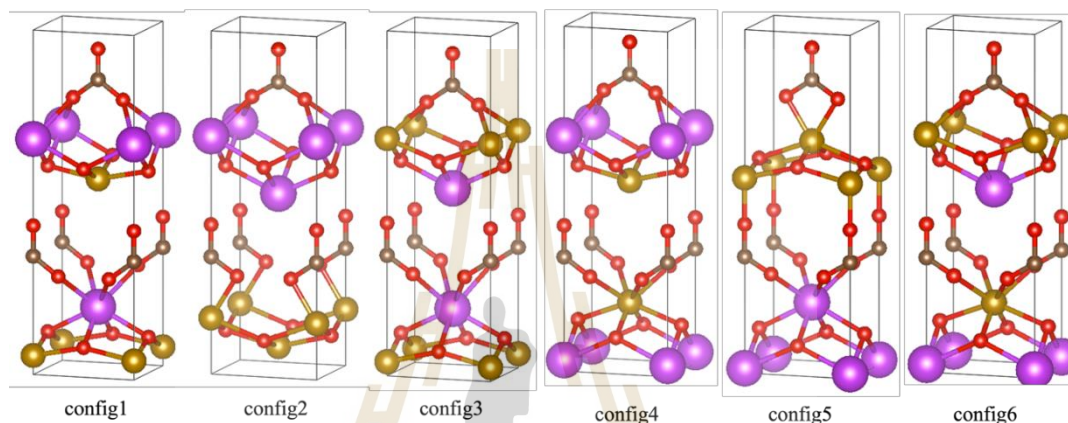
**Figure A-2** All configuration of 50 mol% of Fe-doped in Bi$_2$O$_2$CO$_3$ structure. The magenta, brown, red and grey sphere represent Bi, Fe, O and C atom, respectively.
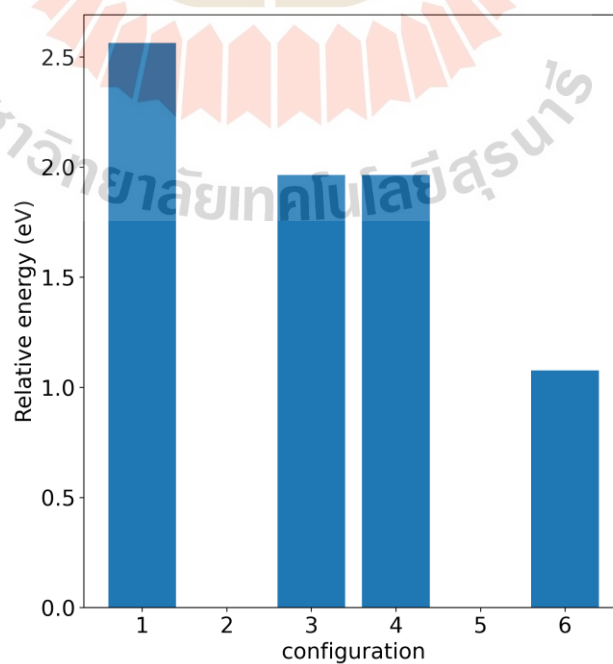


**Figure A-3** The relative total energy of all BiFeO$_2$CO$_3$ configuration.

## 2. Surface energy calculation

For $Bi_2O_2CO_3$ (002) slab model, we consider two configurations as illustrated in Figure A-4. These two slab models used two unit of the bulk $Bi_2O_2CO_3$ structure that contain 8 Bi atoms, 4 C atoms and 20 O atoms with the surface area of 15.940 $Å^2$. The total energy and surface formation energy were listed in Table A-1.
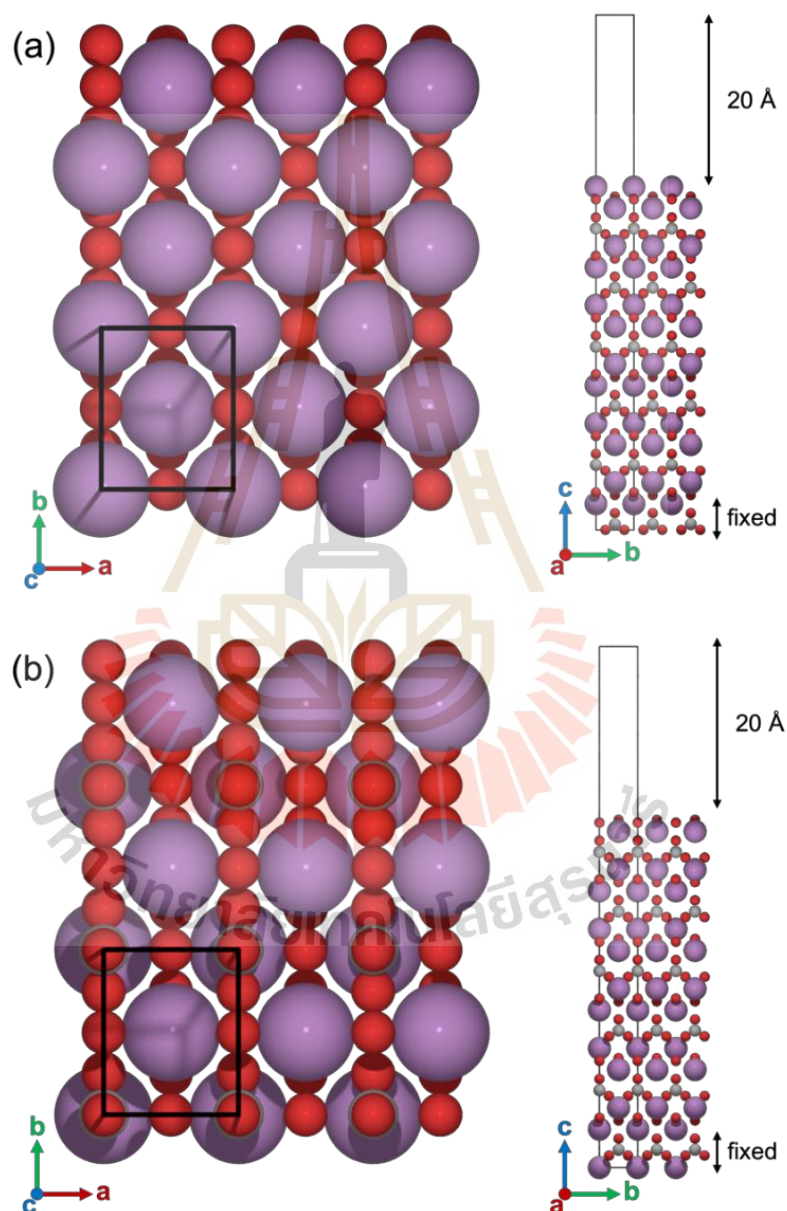


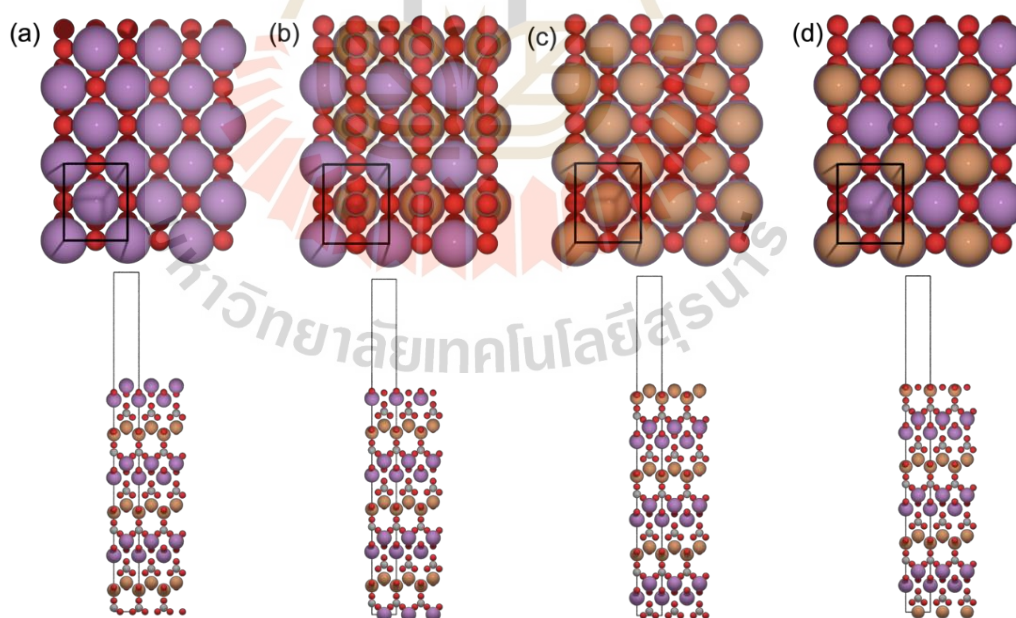**Figure A-4** $Bi_2O_2CO_3$ (002) slab model. (a) surface configuration No.1. (b) surface configuration No.2. The black solid line represents the unit cell of slab model. The magenta, red and grey sphere represent Bi, O and C atom, respectively.

**Table A-1** Total energy, surface area and surface formation energy of $Bi_2O_2CO_3$ structure.

|  | E (eV) | Area ($Å^2$) | $E_{surface}$ (eV/$Å^2$) |
|---|---|---|---|
| bulk | -102.628 | - | - |
| (002) config1 | -202.605 | 15.940 | 0.166 |
| (002) config2 | -200.181 | 15.940 | 0.318 |

To study the surface (002) of for $BiFeO_2CO_3$ structure, the most stable configuration No.5 of bulk $BiFeO_2CO_3$ structure was selected to build a slab model. Four configurations of $BiFeO_2CO_3$(002) were optimized. The $BiFeO_2CO_3$(002) slab model exhibits the surface area of 15.846 $Å^2$. The total energy and surface formation energy was shown in Table A-2.



**Figure A-5** four configurations of $BiFeO_2CO_3$(002) slab model. Configuration No.1, 2, 3 and 4 reflexed in (a), (b), (c) and (d), respectively. The magenta, brown, red and grey sphere represent B, Fe, O and C atom, respectively.

**Table A-2** Total energy, surface area and surface formation energy of $BiFeO_2CO_3$ structure.

|  | E (eV) | Area (Å$^2$) | E$_{surface}$ (eV/Å$^2$) |
|---|---|---|---|
| bulk | -109.868 |  |  |
| (002) config1 | -327.308 | 15.846 | 0.145 |
| (002) config2 | -324.934 | 15.846 | 0.295 |
| (002) config3 | -328.889 | 15.846 | 0.045 |
| (002) config4 | -325.196 | 15.846 | 0.278 |
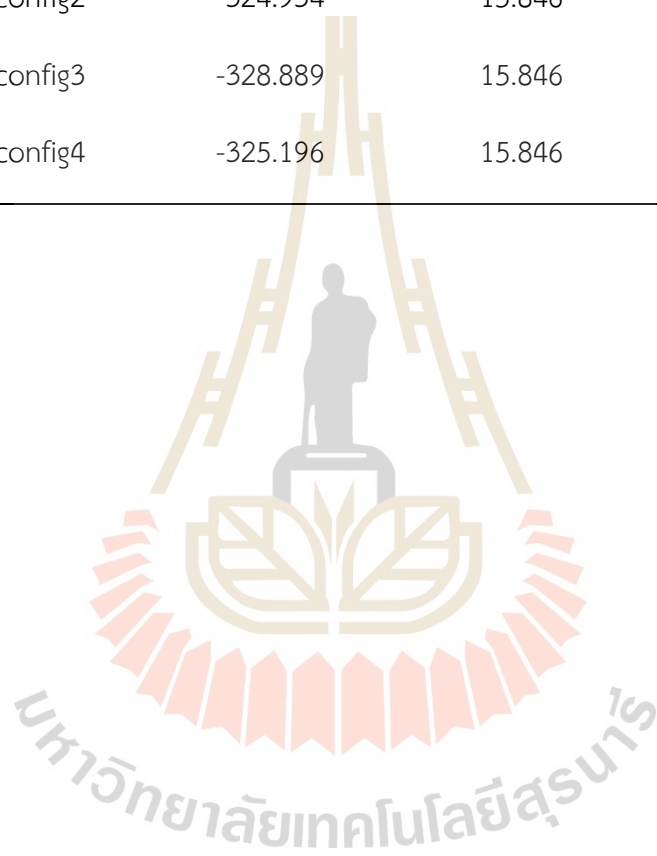
# CURRICULUM VITAE

**Name**            Chaniphon Sunkhunthod

**DATE of Birth**   25$^{th}$ August 1996

**Address**         213 Prajak Raod, Nai-Muang Sub-district, Muang District,
                    Nakhonratchasima 30000

**Education**

2015-2019           B.Sc. (Chemistry), Kasetsart University Sriracha Campus,
                    Thailand

2020-present        Student in M.Sc. Program in Chemistry, Suranaree University of
                    Technology, Thailand